Bioactive Materials 50 (2025) 246–272

Contents lists available at ScienceDirect

Bioactive Materials

journal homepage: www.keaipublishing.com/en/journals/bioactive-materials

A biodegradable, microstructured, electroconductive and nano-integrated drug eluting patch (MENDEP) for myocardial tissue engineering

Caterina Cristallini [a,b,*], Daniela Rossin [c], Roberto Vanni [c], Niccoletta Barbani [b,a], Chiara Bulgheresi [b], Massimiliano Labardi [a], Sadia Perveen [c], Silvia Burchielli [d], Domiziana Terlizzi [d], Claudia Kusmic [e], Silvia Del Ry [e], Manuela Cabiati [e], Cheherazade Trouki [a,f], Dawid Rossino [a,b], Francesca Sergi [b], Anthea Villano [a], Giovanni D. Aquaro [g], Giorgia Scarpellino [h,i], Federico A. Ruffinatti [h], Sara Amorim [j,k], Ricardo A. Pires [j,k], Rui L. Reis [j,k], Raffaella Rastaldo [c,1], Claudia Giachino [c,1]

[a] Institute for Chemical and Physical Processes, CNR-IPCF, Via Giuseppe Moruzzi 1, 56124, Pisa, Italy
[b] Department of Civil and Industrial Engineering, DICI, University of Pisa, Largo Lucio Lazzarino, 56126, Pisa, Italy
[c] Department of Clinical and Biological Sciences, University of Turin, Regione Gonzole 10, 10043, Orbassano, Italy
[d] Fondazione Monasterio, Via Giuseppe Moruzzi 1, 56124, Pisa, Italy
[e] Clinical Physiology Institute, CNR-IFC, Via Giuseppe Moruzzi 1, 56124, Pisa, Italy
[f] Department of Pharmacy, University of Pisa, Via Bonanno 6, 56126, Pisa, Italy
[g] Academic Radiology Unit, Department of Surgical, Medical and Molecular Pathology and of the Critical Area, University of Pisa, Via Paradisa 2, 56124, Pisa, Italy
[h] Department of Life Sciences and Systems Biology, University of Turin, Via Accademia Albertina 13, 10123, Torino, Italy
[i] Department of Biology and Biotechnology "L. Spallanzani", University of Pavia, Via Adolfo Ferrata 9, 27100, Pavia, Italy
[j] 3B's Research Group, I3Bs - Research Institute on Biomaterials, Biodegradables and Biomimetics, University of Minho, Headquarters of the European Institute of Excellence on Tissue Engineering and Regenerative Medicine, AvePark, Parque de Ciência e Tecnologia, Zona Industrial da Gandra, 4805-017, Barco, Guimarães, Portugal
[k] ICVS/3B's-PT Government Associate Laboratory, Braga, Guimarães, Portugal

ARTICLE INFO

Keywords:
Acellular Electroconductive Cardiac Patch
Cardioprotection
Drug delivery
Molecular imprinting
Myocardial infarction
Cardiac regeneration

ABSTRACT

We produced a microstructured, electroconductive and nano-functionalized drug eluting cardiac patch (MENDEP) designed to attract endogenous precursor cells, favor their differentiation and counteract adverse ventricular remodeling *in situ*. MENDEP showed mechanical anisotropy and biaxial strength comparable to porcine myocardium, reduced impedance, controlled biodegradability, molecular recognition ability and controlled drug release activity. *In vitro*, cytocompatibility and cardioinductivity were demonstrated. Migration tests showed the chemoattractive capacity of the patches and conductivity assays showed unaltered cell-cell interactions and cell beating synchronicity. MENDEP was then epicardially implanted in a rat model of ischemia/reperfusion (I/R). Histological, immunofluorescence and biomarker analysis indicated that implantation did not cause damage to the healthy myocardium. After I/R, MENDEP recruited precursor cells into the damaged myocardium and triggered their differentiation towards the vascular lineage. Under the patch, the myocardial tissue appeared well preserved and cardiac gap junctions were correctly distributed at the level of the intercalated discs. The fibrotic area measured in the I/R group was partially reduced in the patch group.

Peer review under the responsibility of editorial board of Bioactive Materials.

* Corresponding author. Institute for Chemical and Physical Processes, CNR-IPCF, Via Giuseppe Moruzzi 1, 56124, Pisa, Italy.
E-mail addresses: caterina.cristallini@cnr.it (C. Cristallini), d.rossin@unito.it (D. Rossin), roberto.vanni@unito.it (R. Vanni), niccoletta.barbani@unipi.it (N. Barbani), chiara.bulgheresi@gmail.com (C. Bulgheresi), massimiliano.labardi@cnr.it (M. Labardi), sadia.perveen@unito.it (S. Perveen), silvia.burchielli@ftgm.it (S. Burchielli), terlizzid90@gmail.com (D. Terlizzi), claudia.kusmic@cnr.it (C. Kusmic), silvia.delry@cnr.it (S. Del Ry), manuela.cabiati@cnr.it (M. Cabiati), cheherazade.trouki@phd.unipi.it (C. Trouki), dawid.rossino@phd.unipi.it (D. Rossino), francesca.sergi22@gmail.com (F. Sergi), antheavillano@gmail.com (A. Villano), giovanni.aquaro@unipi.it (G.D. Aquaro), giorgia.scarpellino@unito.it (G. Scarpellino), federicoalessandro.ruffinatti@unito.it (F.A. Ruffinatti), sara.amorim@i3bs.uminho.pt (S. Amorim), rpires@i3bs.uminho.pt (R.A. Pires), rgreis@dep.uminho.pt (R.L. Reis), raffaella.rastaldo@unito.it (R. Rastaldo), claudia.giachino@unito.it (C. Giachino).
[1] These Authors contributed equally to the work.

https://doi.org/10.1016/j.bioactmat.2025.04.008
Received 4 December 2024; Received in revised form 24 March 2025; Accepted 5 April 2025

Overall, these results demonstrate that MENDEP was fully retained on the epicardial surface of the left ventricle over 4-week implantation period, underwent progressive vascularization, did not perturb the healthy myocardium and showed great potential in repairing the infarcted area.

1. Introduction

Cardiovascular disease is a global cause of morbidity and mortality and is often associated with myocardial infarction (MI) [1]. Adult cardiac tissue is thought to lack the ability to self-repair and regenerate after MI [2].

Current MI treatments, such as drugs and surgical approaches, greatly reduce cardiovascular morbidity and mortality [3]. However, the remodeling process following an acute event frequently leads to arrhythmias and ultimately to heart failure (HF), as those treatments do not restore heart structure and function [4]. In the worst conditions, a heart transplant represents the only option, yet it exhibits several hurdles and a shortage of donors, thereby it cannot be widely adopted.

As a possible alternative, experimental therapies focus on using cells from various origins to promote myocardial regeneration by decreasing the extension of scar area counteracting MI-induced adverse remodeling of the heart [5]. However, their clinical applications for heart repair have several limitations: cell fragility, high cost, possible presence of undifferentiated cells that may become tumorigenic, immunogenicity of allogeneic cells, inadequate electrical and mechanical coupling, and above all, extremely low cell retention and engraftment [6] because of cell death and 'washing away' by the actively contracting heart [7].

The field of *in vivo* cardiac tissue engineering has emerged as a promising alternative strategy for repairing injured cardiac tissue. Cardiac patches, designed to be attached directly to the surface of the heart, are at the forefront of innovation in cardiac surgery [8]. The patches are conceived with the aim of recapitulating microstructure, mechanical properties and molecular signal hubs, i.e., characteristics of healthy native myocardium, to support damaged cardiac tissue in terms of mechanical, cardio-protective and regenerative therapeutic functions.

Despite the promising achievements obtained by worldwide research groups engaged in multifunctional cardiac patches, currently, the cardiovascular patches on the market have only a mechanical function and are mainly made of non-biodegradable polytetrafluoroethylene (PTFE) or biodegradable decellularized animal tissues. The non-biodegradable, synthetic patches exert only mechanical support to avoid the ventricular wall rupture, a rare event with a high risk of mortality that can occur post-MI [9,10]. Decellularized, biological cardiac patches can be employed to repair the injured myocardial tissue and restore its functionality [11]. However, extracellular matrix (ECM) microarchitecture and composition preservation during the decellularization process is a problematic issue [12]. The balance between effective cell removal and preservation of structural, biochemical, and biomechanical properties remains challenging. Due to limitations in the structure's biomimicry, lack of drug-elution ability and low mechanical strength, their application in a clinical setting continues to be challenging [10,12].

These features have been addressed in the design of biodegradable combinations of synthetic polymer/ECM [13], exhibiting significant improvement in heart function restoration, of synthetic polymer/-biological hydrogels [14], or bioartificial polymeric patches [15,16]. However, one of the most important challenges to achieving a proper cardio-inductive and regenerative function of cardiac patches is their poor electrical conductivity. Recently, the focus on the incorporation of conductive materials, including gold nanoparticles, carbon-based nanomaterials, and electroconductive polymers, was addressed [17]. The rationale relies on the need to reduce the impedance typical of the most used polymeric patches to allow the propagation of electrical signals among cardiomyocytes and ultimately the proper contractility of the repaired tissue. Electroactive polymers, like polypyrrole or polyaniline, have received particular attention for their intrinsic conductivity [17–19]. Interesting scaffolds were recently developed that could serve as implantable devices for the treatment and monitoring of cardiac disease once they will be properly implemented [20].

However, one of the main limits for the use of these electroactive polymers is the lack of intrinsic biodegradability, which plays a key role in the proper remodeling of the tissue. Amino acids and short peptides ($n < 5$) modified with the 9-fluorenylmethyloxycarbonyl (Fmoc) moiety have demonstrated the capacity to self-assemble into nanofibers for a wide range of applications [21]. Of note is the ability of these supramolecular nanofibers to copycat the chemical and morphological presentation of proteins and proteoglycans present in the ECM [22]. Moreover, under physiological conditions, these nanofibers can cross-link and generate stable hydrogels that can serve as scaffolds for tissue engineering and regenerative medicine [23,24]. Importantly, the self-assemblies of ultrashort peptides have been proven to present optical and electrical properties comparable to those of conventional inorganic semiconductor materials [25]. One of the most representative bioinspired self-assembling peptides is diphenylalanine (FF) and the introduction of the Fmoc moiety was shown to improve the semiconductivity of the bio-assemblies making them useful for modulating the properties of semiconductor systems [26].

If on the one hand, acellularized scaffolds can be optimized to satisfy the mechanical, electroconductive and biodegradability requirements for correct compliance and integration with the myocardial tissue, on the other hand, they must have the ability to recruit *in situ* the proper endogenous cells thus eliciting regenerative processes. Several molecular mediators, including vascular endothelial growth factor (VEGF), granulocyte-macrophage colony-stimulating factor (GM-CSF), stromal cell-derived factor (SDF-1), and angiopoietin-1 (Ang-1) were demonstrated to enhance the recruitment of circulating progenitor/stem cells and neovascularization in ischemic tissues [27,28]. Acellular scaffolds coupled with these biological molecules offer the potential to drive physiological functions [29].

However, the aforementioned mediators may not be specific for the myocardial repair response [30]. In this regard, particular attention was recently received by an important regulator of the cardiovascular system, named Apelin (and specifically by its biologically active isoform Apelin-13). It is an endogenous ligand that with its G protein-coupled receptor (Aplnr) exerts cardioprotective effects reducing myocardial damage and dysfunction, thus potentially playing a crucial role in tissue repair post-MI [31–33]. Endogenous Apelin also improves pathological remodeling and Ang II-mediated impairment of heart contractility in mice models [34]. It plays a central role in the pathways that regulate positive inotropic and vasodilator effects and exerts cardioprotective activities against I/R injury [35–38]. In addition, Apelin-13 can enhance the mobilization, survival, and proliferation of endogenous myocardial stem cells in the injured heart, thus providing a strategy to repair the heart and improve cardiac function [39]. Moreover, Apelin exerts other biological effects including inflammation reduction and angiogenesis promotion [40,41].

The clinical use of Apelin-13 is however limited because of the instability of this peptide in both *in vitro* and *in vivo* conditions [42]. Nanocarriers can be useful in reducing the rapid degradation of the peptide and its short plasma half-life. For example, a liposomal nanocarrier modified with polyethylene glycol (PEG) was used for its delivery into the injury site of a mouse model showing that the sustained release of apelin attenuates pressure overload-induced cardiac dysfunction [43]. The nano-functionalization includes the use of nanomaterials based on biodegradable polymers to modify cardiac patches as drug delivery systems to treat myocardial ischemia. Among biodegradable

polymers, polyhydroxyalkanoates (PHA) are widely studied as biomaterials due to their specific properties that make them suitable for tissue engineering and drug delivery [44].

One of the most severe complications in myocardial infarction is the left ventricular (LV) remodeling and the control of this process at the level of cardiac ECM is essential for therapeutic approaches in myocardial regeneration. Several studies have shown that following the infarction, an imbalance is created between matrix metalloproteases (MMPs) and their inhibitors, tissue inhibitors of metalloproteinases (TIMPs). The increase in the proteolytic activity of these enzymes facilitates pathological LV remodeling and the dilation of the left ventricle [45].

Conventional treatments often non-specifically inhibit MMP activity, leading to potential off-target effects. Our approach aims to selectively capture excess MMP-9 using molecularly imprinted nanoparticles (MIPs) to restore a physiologically relevant MMP/TIMP balance without broadly suppressing all MMP activity, which is crucial for normal ECM turnover.

Our strategy builds upon prior studies demonstrating the feasibility of MMP-9-targeting MIPs in cardiac scaffolds [46]. Further research expanded on these findings, incorporating computational design, synthesis, and comprehensive physicochemical and biological characterization [47], which collectively validated MMP-9 MIPs as effective, selective binders.

To address the aforementioned challenges, we have developed a multi-level implemented microstructured bioartificial acellular patch (MENDEP) endowed with an electroconductive biodegradable peptide (9-fluorenylmethoxycarbonyl-diphenylalanine, Fmoc-FF), a pleiotropic molecule (Apelin-13) loaded both directly and via biodegradable nanoparticles (NPs), and MIP nanoparticles towards Metalloproteinase-9 (MMP-9). We deeply analyzed the properties of this acellular, clinically feasible, off-the-shelf drug-releasing patch as a potential therapeutic for cardiac repair. To evaluate its early therapeutic impact and biocompatibility, we conducted a 4-week *in vivo* study in a murine I/R-induced MI model. This timeframe was selected based on its relevance for assessing key regenerative processes, such as myocardial repair, inflammatory response modulation, and functional recovery, while ensuring alignment with standard preclinical evaluation protocols for bioartificial cardiac scaffolds. Similar timeframes are commonly used in preclinical studies on cardiac patches, as reported in previous works [48–50]. A 4-week period allows for the assessment of short-to mid-term outcomes, including left ventricular remodeling, vascularization, and biomaterial-host interactions, before significant degradation of biodegradable components occurs.

2. Materials and methods

2.1. Patch characterization

2.1.1. Materials and techniques

All the materials and reagents were obtained from Sigma Aldrich (Milan, Italy), unless otherwise specified. Dimensional and morphological analysis was performed onto gold-sputtered different types of NPs and patches, before and after explant, using a scanning electron microscope (SEM, FEI QuantaTM 450 FEG Instrument, Hillsboro, OR, USA) and Stereomicroscope Leica S9i (Leica microsystem, Wetzlar, Germany). SEM analysis was done at 10 kV in high-vacuum mode, with manual aperture, 2.5 beam spot size, 12,000 and 150,000 magnification and horizontal field width (HFW = 34.5 μm and 2.76 μm). The samples were sputtered with gold to improve the quality of the analyses. μATR and FT-IR Chemical Imaging were conducted using a PerkinElmer Spectrum One FT-IR Spectrometer, equipped with a Universal ATR Sampling Accessory and a Spectrum Spotlight 300 F T-IR Imaging System in "image" mode (PerkinElmer Spotlight 300, Shelton, CT, USA). Each sample, covering a 1 mm × 1 mm area, was analyzed with 25 μm pixel resolution using a liquid nitrogen-cooled 16-pixel mercury cadmium telluride (MCT-A) line detector. Absorbance spectra were recorded for each pixel in the μATR mode in the mid-infrared region (4000–750 cm^{-1}) with a spectral resolution of 4 cm^{-1} over 16 scans per pixel. Specific sample areas were identified using an optical microscope, and the ATR objective collected spectra from the surface layers. The spectra were pre-processed using Spotlight software, including Savitzky-Golay smoothing (9 points). Spectral maps were analyzed to produce a correlation map and band absorbance ratios, assessing chemical homogeneity. The chemical map provided an average spectrum representative of the sample. Band ratio analysis quantified components, and statistical analysis through Principal Component Analysis (PCA) evaluated component distribution. Spotlight software facilitated the generation and interpretation of chemical and correlation maps.

2.1.2. Production and characterization of molecularly imprinted nanoparticles vs MMP-9

By using the precipitation polymerization method, in a diluted condition of methacrylic acid (MAA) monomers in the presence of polyvinylpyrrolidone (PVP), PVP-polymethacrylic acid (PVP-PMAA) MIPs were synthesized according to a template polymerization mechanism. Briefly, MAA and PVP (Mw 20,000 Da) with 1:1 M ratio, trimethylpropane trimethacrylate (TRIM) as cross-linker and Matrix MMP-9 human recombinant (50 ng mL^{-1}) as template were added to PBS solution with pH 7.4, according to the procedure already described in our previous paper [47]. Non-imprinted nanoparticles (CPs) were prepared in the absence of MMP-9 and treated in the same way as MIPs. Finally, the synthesis product is removed and subjected to at least three washing steps to remove the unreacted monomer and the excess PVP. A binary solution of methanol (MeOH)/acetic acid (MeCOOH) (0.1 *v/v* (%) in bidistilled water with a 30:70 *v/v* ratio at 70 °C for 1 h and ethanol (EtOH)/bidistilled water 30:70 *v/v* for 10 min were used for template extraction. Analogue enzymes for selectivity tests were the human recombinant TIMP metallopeptidase inhibitor 1 (TIMP-1) and Matrix Metalloproteinase 2 (MMP-2). The HPLC mobile phase consisted of bidistilled water and acetonitrile (ACN) purchased from Carlo Erba Reagenti (Turin, Italy), with an HPLC purity degree.

TGA was performed on CPs, MIPs, non-extracted NPs (MIPT) and rebound (MIPR) MIPs using a TGA 6 analyzer from PerkinElmer. Small amounts of particles were placed into ceramic capsules and analyzed from 30 °C to 600 °C at a heating rate of 10 °C min^{-1} in nitrogen flow.

HPLC (PerkinElmer Series 200) was utilized to assess the quantity of residual MMP-9 in the reaction batch, as well as in the extraction and rebinding solutions. MIPs and CPs were placed in the rebinding solution (10 ng of MMP-9 in 1 mL of PBS) under dynamic conditions to conduct rebinding tests. A column of C18-Synergy Hydro-RP (Phenomenex, Srl, Castel Maggiore, Bologna, Italy) was employed. Operating conditions of the HPLC analysis: a mobile phase of ACN/bidistilled water (07/93 *v/v*); a flow rate of 0.8 mL min^{-1}; an injection volume of 100 μl by autosampler and the UV detector set at λ = 210 nm.

The experimental data were related to two fitting curves using kinetic models of pseudo-first order and pseudo-second order [51]. The expressions of two models are obtained by integrating the following general equation:

$$\frac{dQ_t}{dt} = k_n(Q_e - Q_t)^n$$

where Q_e (μg g^{-1}) and Q_t (μg g^{-1}) indicate the value of μg of enzyme linked by 1 g of NPs respectively at equilibrium and at time *t* (min); k_n is the kinetic constant of the adsorption reaction. Pseudo-first order reaction, $n = 1$ and the kinetic constant is expressed in min^{-1}, pseudo-second order reaction, $n = 2$ and the kinetic constant is expressed in $\mu g^{-1} g\ min^{-1}$. By integrating the above equation and imposing that, at time $t = 0$, $Q_t = 0$ and at time $t = t$, $Q_t = Q_t$, the following equations of the pseudo-first and pseudo-second order are obtained:

$$Q_t = Q_e\ (1 - e^{-k_1 t})$$

$$Q_t = \frac{k_2 t {Q_e}^2}{1 + k_2 t Q_e}$$

MIP selectivity vs MMP-9 was evaluated by placing MIPs into aqueous solutions containing TIMP-1 or MMP-2, and after ultracentrifugation by analyzing the supernatant using HPLC to evaluate the residual amounts of enzymes.

2.1.3. Production and characterization of PHB nanoparticles

20 mg of Polyhydroxybutyrate (PHB) were introduced into 1 mL of acetone (ACT), this mixture was added dropwise into 8 mL of Polyvinyl alcohol (PVA) 0.1 *w/v* (%), used as a surfactant, and mechanically stirred for 16 h at 700 rpm. The PVA excess was removed by three washing steps in bidistilled water followed by filtering with a 0.2 μm filter. The PHB NPs were obtained after drying in the oven. PHB NPs were loaded with (Glp1)-Apelin-13 (trifluoroacetate salt, M_W 1533.8 Da, Cayman Chemical from Vinci-Biochem Srl, Firenze, Italy). In particular, 3 mg of NPs with 1 mL of Apelin-13 solution 0.05 mM were left for 2 h under stirring at room temperature. Then, PHB NPs loaded were separated by ultracentrifugation from the Apelin-13 solution and dried under a hood at room temperature. SEM analysis was carried out on PHB NPs before and after Apelin-13 loading. An aliquot of PHB NPs loaded with Apelin-13 was poured directly on a microscope slide and analyzed by FT-IR Chemical Imaging allowing us to evaluate the presence of Apelin-13 in the particle aggregates.

2.1.4. Preparation and characterization of MENDEP

Poly(DL-lactide-co-glycolide) (PLGA) with a ratio of lactide to glycolide of 50:50 and a molecular weight of 40–75 kDa, Gelatin derived from porcine skin, dichloromethane (DCM), ACT, and tetrahydrofuran (THF) were purchased from Carlo Erba Reagenti (Turin, Italy). 9-fluorenylmethoxycarbonyl-diphenylalanine (Fmoc-FF) was provided by Biogelx Ltd, Scotland, UK. The external microstructured PLGA/Gelatin/Fmoc-FF membranes (m-MEP), according to the predefined geometry in PDMS molds [15,16], were prepared starting from solutions of Gelatin in bidistilled water at 10 *w/v* (%) and of PLGA at 10 *w/v* (%) in DCM and ACT; the oligomer Fmoc-FF was previously dissolved at 0.025 *w/v* (%) in ACT portion. Gelatin solution was added to the PLGA/Fmoc-FF solution to have a PLGA/Gelatin ratio of 70:30 *w/w*. The final PLGA/Gelatin/Fmoc-FF blend was deposited on PDMS molds and dried for 24 h under a ventilated hood. Each single microstructured layer was gently removed from the mold. Both external layers were sterilized as previously described [15,16]. The intermediate layer consists of Fmoc-FF hydrogel loaded with Apelin-13: an aliquot of Fmoc-FF was dissolved in bidistilled water at pH 12 followed by sonication for 15 min and the addition of a volume of HCl such as to adjust the pH of the solution up to 7.5–8.5. The resulting gel, at a final concentration of 10 mM, was kept in the fridge for 24 h. A predefined volume of 0.05 mM of Apelin-13 solution was introduced into the hydrogel. To form the final structure of the patch, 1 mL of hydrogel, loaded with Apelin-13, was deposited on the membrane from the non-microstructured side, and subsequently, a second membrane was placed over the hydrogel, exposing its microstructured side to the outside. The assembly (MEDEP) was performed by fixing the edges of the patch using a system with sharp blades (specially designed with variable dimensions), preheated to allow for simultaneous cutting and welding. The MMP-9-MIPs and PHB NPs loaded with Apelin-13 were both dispersed in a mixture of water/-ethanol (30:70 *v/v*), sonicated and sprayed onto the patch on both microstructured sides until reaching a deposition density of about 10 μg per cm^2 and 3.4 μg per cm^2, respectively. A schematic of the Microstructured Electroconductive Nano-functionalized Drug Eluting Patch (MENDEP) is reported in Fig. 1. Additional control samples were prepared and used for the *in vitro* tests, as summarized in Table 1.

Dynamic mechanical analysis was performed by DMA (DMA8000, PerkinElmer, USA), using strain scan analysis by applying a sinusoidal deformation at 1, 2, and 3 Hz frequencies (n = 6). Storage modulus (E′), loss modulus (E′′) and loss factor (tanδ) for MENDEP were evaluated in dry and wet conditions at 37 °C, applying the strain in parallel and perpendicular directions. DMA analysis was also carried out on samples left to degrade in PBS for 4 and 7 days at 1 Hz frequency.

Tensile tests, suture tests and burst strength tests were performed by INSTRON (model 5500R-1185,825, Norwood, MA, USA) equipped with a 100 N load cell (n = 6). The samples subjected to tensile and suture tests were tested in dry and wet conditions (after 25 min in PBS), both in the longitudinal and transverse direction. Tensile tests were carried out on patch specimens (28 mm × 8 mm × 1 mm) with a constant deformation of 10 mm min^{-1}, sampling time every 10 ms. Suture resistance tests were performed using ISO 7198:2017 for cardiovascular implants. This test was carried out on patch specimens (20 mm × 8 mm × 1 mm); the suture point using silk thread (Ethicon Inc. 3-0) was inserted 2 mm from the end of the patch, and the suture was held by the upper clamp

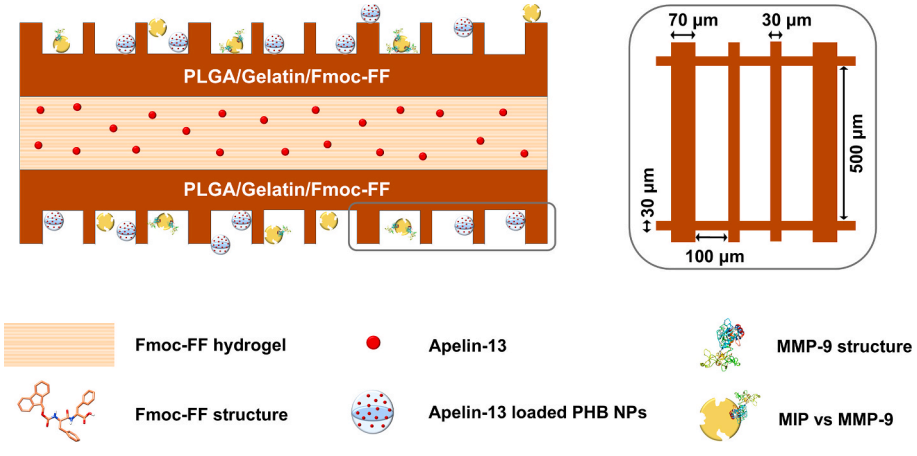

Fig. 1. Schematics of the Microstructured Electroconductive Nano-functionalized Drug Eluting Patch (MENDEP). The patch is designed to include two external microstructured and bioartificial polymeric membranes (PLGA/Gelatin) to provide a biomimetic and biodegradable interface for cardiac tissue growth and a semiconductive peptide (Fmoc-FF) to enhance patch electroconductivity. The incorporation of Fmoc-FF into the external membranes and of a Fmoc-FF hydrogel as an internal layer enables the electromechanical coupling with the surrounding cardiac microenvironment. The Fmoc-FF hydrogel is loaded with Apelin-13 that may promote a large set of biological activities including stem cell recruitment, cardioinductivity, cardioprotection, and antifibrotic effect. Deposition on the external surfaces of the patch of PHB NPs loaded with Apelin-13 enables control over the release of the drug and favors its protection against degradation by endo-proteases. A second class of NPs deposited onto the external surfaces, MIPs imprinted towards MMP-9, are designed to reduce the left ventricular remodeling.

Table 1
Explanation of the acronyms of the various patches and controls considered in this work.

m-PLGA	Single microstructured membrane of PLGA
m-MP	Single **m**embrane of **M**icrostructured **P**atch (PLGA/Gelatin)
MP	**M**icrostructured **P**atch: PLGA/Gelatin bilayer with an intermediate layer of Gelatin hydrogel
MEP	**M**icrostructured **E**lectroconductive **P**atch: PLGA/Gelatin/Fmoc-FF bilayer with an intermediate layer of Fmoc-FF hydrogel
MEP + Ape-NPs	**M**icrostructured **E**lectroconductive **P**atch + **Ape**lin-**N**ano**P**articles: PLGA/Gelatin/Fmoc-FF bilayer with an intermediate layer of Fmoc-FF hydrogel + PHB nanoparticles loaded with Apelin-13
MEP + MIPs	**M**icrostructured **E**lectroconductive **P**atch + **M**olecularly **I**mprinted **P**articles: PLGA/Gelatin/Fmoc-FF bilayer with an intermediate layer of Fmoc-FF hydrogel + MIPs vs MMP-9
MEDEP	**M**icrostructured **E**lectroconductive **D**rug **E**luting Patch: PLGA/Gelatin/Fmoc-FF bilayer with an intermediate layer of Fmoc-FF/Apelin-13 hydrogel + PHB nanoparticles loaded with Apelin-13 + MIPs vs MMP-9
MNDEP	**M**icrostructured **N**ano-functionalized **D**rug **E**luting **P**atch: PLGA/Gelatin bilayer with an intermediate layer of Gelatin/Apelin-13 hydrogel + PHB nanoparticles loaded with Apelin-13 + MIPs vs MMP-9
MENDEP	**M**icrostructured **E**lectroconductive **N**ano-functionalized **D**rug **E**luting **P**atch: PLGA/Gelatin/Fmoc-FF bilayer with an intermediate layer of Fmoc-FF/Apelin-13 hydrogel + PHB nanoparticles loaded with Apelin-13 + MIPs vs MMP-9

and subjected to uniaxial tensile test. The raw force-displacement data were converted to force-strain. The deformation was calculated as follows: $\varepsilon = \Delta L \cdot L_0^{-1}$, where L_0 is the initial length, i.e., the distance between the lower clamp and the suture point, while ΔL is the displacement of the upper clamp. The ISO specifies that the maximum force must be greater than the minimum one specified by the manufacturer.

The burst resistance test was performed to simulate the biaxial forces to which the patch is subjected *in vivo* and to determine its resistance when subjected to significant load conditions. A specific test apparatus was designed using Solidworks 3D CAD software, consisting of a probe able to perforate the sample held in position by the ring in the support base. Compression tests were performed fixing the apparatus to INSTRON using 16 mm diameter samples. The probe displacement speed was set to 50 mm min $^{-1}$ (ISO 7198:2017) and the sampling time was every 2 ms (Figures S1G, H and I).

Degradation tests were performed on MENDEP in PBS pH 7.4 at 37 °C to evaluate degradation kinetics in terms of both weight loss over time and variation over time of the weight averaged (Mw) and numeral (Mn) molecular weight. Gel permeation chromatography (GPC, PerkinElmer, USA) analysis was carried out to evaluate the molecular weight decrease of patch specimens. For GPC analysis, a PerkinElmer pump, equipped with a ResiPore (Agilent Technologies, USA) column, using UV and RI detectors, was used. Operating conditions of the GPC analysis: a mobile phase of THF; a flow rate of 1 mL min^{-1}; injection volume 100 μl; and the UV detector set at λ = 245 nm; room temperature; calibration curve obtained with polystyrene narrow standards.

Conductivity analysis was carried out to study the patch properties, using an impedance spectrometer (Alpha analyser, Novocontrol GmbH, Darmstadt, Germany). Samples of patches (0.9 cm diameter) with Fmoc-FF (MENDEP), without Fmoc-FF (MNDEP), MP and m-MP as controls, were surrounded by a Teflon ring and covered by two metallic plates to contain the pre-swelled samples in bidistilled water for 30 min, and to maintain the thickness of the sample constant during the test. Electrical impedance was measured as a function of frequency in a broad frequency range, including frequencies from 0.1 to 100 Hz that are the most relevant for the intended application. Measurements were repeated at least twice to check stability of the system.

Release tests of Apelin-13 from MENDEP were conducted in PBS at 37 °C under constant stirring and were performed by HPLC (PerkinElmer Series 200), equipped by an Aeris 3.6 μm WIDEPORE XB-C8 column (Phenomenex, S.r.l., Italy). Operating conditions of the HPLC analysis: a mobile phase of ACN/bidistilled water (80/20 *v/v*); a flow rate of 1 mL min^{-1}; an injection volume of 100 μl by autosampler and the UV detector set at λ = 215 nm.

2.2. In vitro biological assays

2.2.1. Cell culture

H9C2 cardiomyoblasts and human mesenchymal stem cells (hMSCs), isolated from the bone marrow of healthy donors, were commercially purchased from the American Type Culture Collection (ATCC, Manassas, VA, USA) and cultured in low glucose DMEM supplemented with 1 % sodium pyruvate, 1 % nonessential amino acids, 1 % kanamycin, 1 % L-glutamine, and 10 % FBS (all from Sigma-Aldrich, Milan, Italy), and kept in an atmosphere of 5 % CO_2, 95 % air at 37 °C in a humidified incubator. Cells were expanded at a seeding density of 3.5 × 10^4 cells per cm^2 and subcultured twice a week.

The isolation and characterization of rat cardiac resident non-myocyte cells (rNMCs) were carried out using a previously established method [52]. The rNMCs were obtained from male Wistar rat hearts and cultured in α-MEM (Sigma-Aldrich, Milan, Italy) supplemented with 2 mmol l^{-1} L-glutamine, 100 U mL^{-1} penicillin, 100 μg mL^{-1} streptomycin and 0.5 % or 10 % FBS. The cells were incubated at 37 °C in a humidified atmosphere of 5 % CO_2 and 95 % air and utilized for the experiments during passage 1–2.

The Cardiomyocytes derived from Human induced Pluripotent Stem Cells (hiPSC-CMs) were obtained from PluriCell Biotech (now LizarBio, Campinas, Brazil). These cells were cultured in RPMI medium (Gibco provided by ThermoFisher Scientific, Monza, Italy) supplemented with 1X B27, 1 % kanamycin and 10 μM rock inhibitor (Sigma-Aldrich, Milan, Italy). The hiPSC-CMs were kept in a humidified incubator with 5 % CO_2 and 95 % air, at 37 °C. Depending on the experimental requirements, the cells were cultured on glass coverslips, on patches or in 96 wells flat bottom plates previously coated with Fibronectin (50 μg mL^{-1}, Sigma-Aldrich, Milan, Italy) to facilitate cell adhesion. hiPSC-CMs beating was recorded by using the inverted microscope Motic AE 2000 and elaborated with Motic Images Plus 3.4 Software (Motic, Richmond, BC, Canada). Cell sheets were produced using temperature-responsive culture dishes (Thermo Scientific Nunc UpCell Surface, Monza, Italy). 2.5 × 10^5 (about 30 %) H9C2 cells and 5.5 × 10^5 (about 70 %) rNMCs were resuspended in 500 μL of complete α-MEM and seeded in 48 well UpCell plates. After 24 h, UpCell plates were placed at 20 °C (room temperature) and after 15 min cells were detached as cell sheets. Cell sheets were collected and placed on the surface of MENDEPs (0.38 cm^2) in 24-well plates.

The THP-1 human monocytic leukemia cell line was purchased from ATCC (Manassas, VA, USA) and cultured in RPMI medium (Gibco, Grand Island, NY, USA) supplemented with 10 % FBS, 1 % kanamycin (Sigma-Aldrich, Milan, Italy), and 0.05 mM 2-mercaptoethanol (Gibco, #21985023). The cells were kept in an atmosphere of 5 % CO_2, 95 % air at 37 °C in a humidified incubator.

2.2.2. Cytocompatibility and skin sensitizing potential tests

Cytocompatibility analysis of PHB and MIPs, covering a broad range of doses, was carried out using Propidium Iodide (PI) Flow Cytometry assay and H9C2 cells. The cells were seeded in 24-well plates, with 5 × 10^4, 4 × 10^4, and 2.5 × 10^4 cells per well for three different exposure periods (24, 48, and 72 h). Negative controls were cells seeded alone. 24 h after seeding, each well's culture medium was removed and replaced with 800 μl of fresh culture medium and 200 μl of sterile PHB and MIP with various final concentrations (0.64, 6.4, 12.8 and 64 mg mL^{-1}).

For scaffold cytocompatibility analysis, H9C2 cells (3 × 10^4 cells) and hMSCs (2 × 10^4 cells) were cultured with MENDEP, and negative

control cells were seeded alone. Following 24, 48, and 72 h of culture, cells were detached with Trypsin-0.2 % EDTA, resuspended in 500 μl of cold 1X PBS (Sigma-Aldrich, Milan, Italy), and transferred into falcon tubes for flow cytometry analysis. Then, 10 μl of PI (1:20 in bidistilled water, Sigma-Aldrich, Milan, Italy) were added, and after 5 min, cell viability was investigated with CyAN ADP flow cytometer (Beckman Coulter, Brea, CA, USA) and analyzed by Summit 4.3 software. The experiments were conducted twice, with triplicates for each condition.

A human cell line activation test (h-CLAT) was carried out to assess the skin sensitizing potential of MENDEP by evaluating the expression levels of CD54 and CD86 membrane markers in the THP-1 human monocytic leukemia cell line, according to OECD 442E and EURL –ECVAM protocol. THP-1 cells were seeded in 96-well plates at 1×10^5 cells mL^{-1} and exposed for 24h to MENDEP eluate, obtained by incubating the solid patch overnight at 37 °C in culture medium. The eluate was serially diluted, with final test concentrations ranging from 39.1 to 6001.8 μg mL^{-1}. Culture medium was used as a negative control, while the contact sensitizing agent 2,4-Dinitrochlorobenzene (DNCB, 4 μg mL^{-1} from Sigma-Aldrich Srl, Milan, Italy) served as a positive control. After incubation, cells were washed, resuspended in FACS buffer, blocked with γ-globulins (Sigma-Aldrich Srl, Milan, Italy), and then stained with fluorescent antibodies against CD86 and CD54 (Bio-Sciences, Milan, Italy) or IgG1 isotype controls (Sigma-Aldrich Srl, Milan, Italy). PI staining assessed cell viability, and flow cytometry measured CD86 and CD54 expression. The Relative Fluorescence Intensity (RFI) was calculated on the geometric mean fluorescence intensity (MFI) as indicated by the formula:

$$RFI = \left(\frac{MFI\,chemical treated\,cells - MFI\,chemical treated\,isotype\,control}{MFI\,solvent treated\,cells - MFI\,solvent isotype\,control} \right) x100$$

Cut-off for positivity were adapted from h-CLAT criteria (CD86 ≥ 150 % and/or CD54 ≥ 200 %).

A substance is classified as a sensitizer if two independent runs show positive upregulation of CD54 and/or CD86, since their increasing expression level on monocytes is a signal of activation of immune response.

2.2.3. Cell migration assay

rNMCs and hMSCs were seeded on polyethylene terephthalate (PET) membranes of 24-well BD Falcon culture inserts (6.5 mm diameter of insert, 8.0 μm pore size of membrane Falcon by Corning, New York, NY, USA) at the final density of 5×10^4 cell per cm^2 and 1×10^4 cell per cm^2, respectively, in DMEM supplemented with 0.5 % FBS. Fibronectin (Sigma-Aldrich Srl, Milan, Italy) 50 μg mL^{-1} coating on membranes was performed by incubating the inserts for 2h at 37 °C in a humidified 5 % CO_2 atmosphere. Inserts were placed in 24 well plates, and the lower chambers of 24-well systems were filled with 600 μL of DMEM 0.5 % FBS (negative control), DMEM 0.5 % FBS with (Glp1)-Apelin-13 (Cayman Chemical from Vinci-Biochem Srl, Firenze, Italy) 100 nM (soluble factor), and DMEM 0.5 % with different patches (MEP + Ape-NPs, MEP + MIPs, MEDEP and MENDEP). The multiwells containing the cell culture inserts were incubated at 37 °C in a humidified 5 % CO_2 atmosphere and migration assays were carried out for 24h. Afterwards, culture inserts were rinsed with PBS and cells attached to the upper side of the membrane were mechanically removed by a cotton-tipped applicator. Cells that migrated to the lower side of the membrane were fixed by treating with 2.5 % glutaraldehyde for 30 min at RT and stained with 2 % crystal violet for 1h at RT. For each insert, five random fields were acquired with an inverted microscope Motic AE 2000 (Motic, Richmond, BC, Canada). Finally, the cells were counted by ImageJ ® software (USA, http://rsb.info.nih.gov/ij/) and the total number of migrated cells per membrane was calculated.

2.2.4. Seeding and culture of cells on MENDEPs

Depending on the experiments, between 5×10^3 and 20×10^3 cells were resuspended in 50 μl of complete α-Minimum Essential Medium (MEM) or DMEM or RPMI supplemented with 10 % fetal bovine serum (FBS, Euroclone, Milan, Italy) and seeded in drops on the surface of MENDEPs placed in 24-well plates. After 3 h necessary for cell adhesion, 500 μl of complete medium were added to cover the scaffolds and then samples were kept in an atmosphere of 5 % CO_2, and 95 % air at 37 °C in a humidified incubator. Cells seeded on the scaffolds were maintained in culture for 1–4 weeks and the medium was replaced every 2 days. For 2D control condition, between 1.5×10^3 cells per cm^2 and 4×10^3 cells per cm^2 were seeded and harvested at 80 % confluence.

2.2.5. Cell morphology and alignment analysis

For immunofluorescence analysis of cell morphology, cytoskeletal organization and colonization of MENDEPs, cellularized scaffolds were processed at room temperature. Briefly, samples were washed twice with PBS and subsequently fixed with 4 % paraformaldehyde (PAF, Sigma-Aldrich, Milan, Italy) for 30 min, before permeabilizing with 0.1 % Triton X-100 for 15 min and blocking with 6 % bovine serum albumin (BSA, Sigma-Aldrich, Milan, Italy) and 2.5 % normal goat serum (NGS, Sigma-Aldrich, Milan, Italy) for 1 h. Actin filaments were then stained with an anti-Vinculin antibody for 2 h at RT (1:400, V9131, Sigma-Aldrich, Milan, Italy) followed by an Alexa Fluor 488 for 1 h at RT (1:400, A11070, Invitrogen, Thermo Fisher, Monza, Italy) as secondary antibody and with Tritc-phalloidin 1:200 for 2 h at RT (Sigma-Aldrich, Milan, Italy). Nuclei were counterstained with 4′-6-Diamidino-2-phenylindole (DAPI) (1:2500, Sigma-Aldrich, Milan, Italy) for 30 min. After mounting on glass slides with Mowiol aqueous solution (Calbiochem, San Diego, CA, USA), cellularized scaffolds were analyzed by confocal microscopy (TCS-SPE, Leica Microsystem, Wetzar, Germany).

Cell alignment and elongation were evaluated with Calcein-AM (Sigma-Aldrich, Milan, Italy), a cell-permeant molecule, which is cleaved by intracellular esterases to produce a green fluorescent dye that is retained in the cytosol of living cells. Cellularized scaffolds were stained with 2 μmol l^{-1} Calcein-AM for 30 min at 37 °C and then analyzed by confocal microscopy (Carl Zeiss Laser Scanning System LSM 510, Oberkochen, Germany). The staining was repeated on the same scaffolds at 1, 4, 8, 12 and 15 days of culture.

3D reconstructions were obtained with Zen 3.4 Blue Edition (Carl Zeiss Laser Scanning System LSM 510, Oberkochen, Germany).

2.2.6. RNA extraction, cDNA synthesis, qPCR, ddPCR

Cellularized patches (MEP + Ape-NPs, MEP + MIPs and MENDEP) were dissolved in TRIzol reagent (Thermo Fisher Scientific, Monza, Italy) and total RNA (totRNA) was extracted according to the manufacturer's instructions. Genomic DNA contaminations were removed by DnaseI treatment (Sigma-Aldrich Srl, Milan, Italy) and RNA was quantified with NanoDrop™ ND-1000 spectrophotometer (Euroclone, Milan, Italy). One microgram of totRNA was retrotranscribed with random hexamer primers and Multiscribe Reverse Transcriptase contained in the High-Capacity Reverse Transcription Kit (Thermo Fisher Scientific, Monza, Italy) following the manufacturer's suggestions.

Expression levels of target genes and reference genes were evaluated with SYBER green technology on an ABI PRISM 7500 Fast Real-Time PCR system (Thermo Fisher Scientific, Monza, Italy) using 25 ng of cDNA template and 150 μM of each primer (listed in Table S3). Melting curve analysis was performed for all amplicons. For each target gene, fold change in expression levels between cellularized scaffolds and 2D control culture was evaluated with the $2^{-\Delta\Delta Ct}$ method using either UBC or Polr2A as a reference gene and matched 2D control culture as calibrators.

The comparison between MENDEP and patches with single functionalization was performed by using ddPCR™. Each sample was partitioned into ~20,000 droplets by a droplet generator (QX200™ Droplet Generator, Bio-Rad, Hercules, CA, USA) and each droplet was amplified by using ddPCR™ Supermix Evagreen (Bio-Rad, Hercules, CA, USA) and the thermal cycling conditions suggested by the manufacturer. Primers

were used at a final concentration of 100 nM. After the amplification, each sample was loaded onto the QX200™ Droplet Reader (Bio-Rad, Hercules, CA, USA), and ddPCR data were analyzed with QX Manager™ analysis software (version 2.0, Bio-Rad, Hercules, CA, USA). The target concentration in each sample was expressed and normalized as a percentage of gene/*UBC* (Gene Ratio); the differential expression was evaluated relative to 2D control culture and expressed as base 2 log of fold change ($\log_2$(Gene Ratio$_{[\text{conc x}]}$/Gene Ratio$_{[\text{ctrl}]}$)).

2.2.7. Calcium imaging

After 24 h, hiPSC-CMs cultured on MENDEP were loaded with 5 μM Fura-2AM ratiometric calcium probe (Invitrogen, Carlsbad, CA, USA) for 30 min in incubator (37 °C; 5 % CO_2) and fluorescence was acquired by Nikon Eclipse TE-2000S (Minato, Tokyo, Japan) inverted microscope and Metafluor Imaging System (Molecular Devices, Sunnyvale, CA, USA). The samples were excited at 340 nm and 380 nm alternatively, and the intracellular calcium concentration ($[Ca^{2+}]_i$) was expressed as a ratio (R) of the fluorescence at 510 nm corresponding to the two excitation wavelengths. For each condition, at least three independent experiments were performed, selecting at least 20 regions of interest (ROIs) per experiment. In each run, images were background-subtracted and acquired every 500 ms for at least 15 min. The first 750 s of each time course were then analyzed using a homemade GNU Octave/MATLAB script for the quantitative characterization of calcium dynamics. Specifically, for each experiment, the mean value of basal calcium levels (field-averaged basal $[Ca^{2+}]_i$)was assessed. To address the oscillatory component of the signals, spike amplitude was then taken into account in terms of both per-experiment mean value and intercellular variability. Finally, the time-averaged $[Ca^{2+}]_i$ spiking rate was evaluated for each experiment. These four quantitative descriptors were separately used to statistically compare calcium signals from hiPSC-CMs cultured on MEP + Ape-NPs and MENDEP with those from the same cells in control conditions. Algorithmic details can be found on the GitHub Gist public repository at gist.github.com/Feat-FeAR/ceedb42bd27d67601afe681cd0dea43c, where the GNU Octave/MATLAB code can be inspected and downloaded.

2.3. Experimental design and in vivo validation

2.3.1. I/R animal model

The *in vivo* experimental activity on the rat animal model was performed at the Centro di Biomedicina Sperimentale (CBS), Research Area of the CNR (Pisa, Italy), after authorization no. 536/2020-PR on May 27, 2020 delivered by the Experimental Animal Ethics Committee of the Italian Ministry of Health. 32 male Wistar rats (4 months of age; 260–426 g of body weight) were used, randomly divided into four main experimental groups: Sham (S): control group, thoracotomy without ligation of the left anterior descendent coronary artery (LAD); Sham + Patch: thoracotomy without ligation of LAD and positioning of the patch; I/R, thoracotomy and LAD occlusion for 30 min without any treatment; I/R + P: thoracotomy and LAD occlusion for 30 min and patch placement after 10 min from occlusion.

To perform the surgical intervention, each animal was subjected to the following treatments in sequential order: general anesthesia (Zoletil® 40 mg kg^{-1}, Xylazine 7.5 mg kg^{-1}) preventive analgesic therapy (Carprofen 5 mg kg^{-1}), orotracheal intubation and placement of 4 plate electrodes at the extremity of each limb for electrocardiographic monitoring.

With the animal in dorsal decubitus, after shaving the left hemithorax and cleansing with betadine and neoxidine, the left thoracic cavity was opened with an incision of the muscles at the level of the 5th intercostal space after which the animal was connected to the respirator (tidal volume of 8 mL kg^{-1}, respiratory rate of 90) and maintained in mechanical respiration until the end of the surgical procedure.

After opening the pericardial sac and instilling lidocaine on the epicardium, a suture (Vicryl 5/0) was passed through the epicardium layer around the LAD about 2–3 mm from its origin. LAD was occluded for 30 min (period of ischemia) by tying a loop, then the knot around the vessel was opened and unrestrained reperfusion was allowed. The Sham group underwent all surgical procedures except for the occlusion of the LAD.

In the Sham + P and I/R + P (after 10 min of occlusion) groups, the patch, previously hydrated with sterile physiological solution, was sutured at the center with a single stitch (Vicryl 5/0) on LV wall in correspondence with the infarcted area.

At the end of the 30 min, the chest was closed, under suction, with detached sutures of Prolene 3/0 for the muscular part and Vicryl 2/0 for the skin. The animal was progressively weaned from mechanical ventilation and when in spontaneous breathing positioned on a heated mattress until complete recovery and then repositioned in its own cage. Antibiotic therapy (Baytril® 2.5 % oral sol) was maintained for one week, while analgesic therapy (acetylsalicylic acid drops 100 mg kg^{-1}) for three days or until needed.

2.3.2. Electrocardiographic monitoring and magnetic resonance imaging

During the surgery, the electrocardiographic signal in the three standard leads D1-D2-D3 was recorded on paper at the following time points: T0, after intubation and positioning in dorsal decubitus; T1, after the passage of the thread incorporating the LAD with and without ischemia; T2, after applying the Patch where required; T3, after removal of the thread (reperfusion where foreseen); T4, after surgical closure of the thorax.

During the post-operative phase (7, 14, 21 and 30 days), electrocardiographic examinations were performed after gas anesthesia (isoflurane 1–2 % in 100 % oxygen) through a mask and in spontaneous breath every week until sacrifice.

Cardiac magnetic resonance imaging (cMRI) was performed at 1 and 4 weeks after surgery, on a reduced number of animals. The examination was performed following general intraperitoneal anesthesia (Zoletil® 40 mg/kg, Xylazine 7.5 mg/kg) and cannulation of the caudal vein. cMRI was performed to visualize the beating heart and to evaluate the structural/functional parameters, including the ejection fraction and stroke volume.

2.3.3. Explant

Last, animals were euthanized and the specimens, along with the adjacent tissues, were collected for further examination. Blinded analyses were always performed. The explant was performed with a beating heart with the animal under terminal anesthesia.

The harvested hearts were washed in ice-cold saline solution and then, they were dissected to obtain two cups of the ventricles through a short axis midplane cut. In some animals implanted with patches, of both I/R and Sham groups, the patch was left *in situ*, while in other rats the patch was removed and frozen for SEM and FT-IR chemical imaging analyses. For all the hearts, half cup tissue, containing the apex, was immediately soaked in RNA later solution for the subsequent biomolecular analyses. The half cup containing the base was fixed in 10 % buffered formalin for 48–72 h for histopathological analyses. Samples were then dehydrated through graded alcohol series, cleared in xylene and embedded in paraffin wax (melting point 56 °C). Serial sections of 5 μm were cut, placed on slides and heated at 40 °C overnight.

2.3.4. Molecular analysis of explants

Cardiac tissue harvested by the border, remote and infarct zones was homogenized as described in a previous study of ours [53]. Briefly, they were homogenized with a guanidinium thiocyanate-phenol solution (Qiazol® Qiagen S.p.A, Milan, Italy) and RNA was purified using a dedicated assay (miRneasy Mini kit, Qiagen, Milan, Italy). High-quality RNA was eluted in 80 μl volume of RNase-free water; all RNA samples were stored at −80 °C after integrity, purity and concentration evaluation. First-strand cDNA was synthesized with an iScript cDNA Synthesis kit (Bio-Rad, Hercules, CA, USA) and the cDNA samples obtained were placed on ice and stored at 4 °C until further use.

Real-time PCR analysis was performed in duplicate in the Bio-Rad C1000™ thermal cycler (CFX-96 Real-Time PCR detection systems, Bio-Rad Laboratories Inc., Hercules, CA, USA). using a fluorogenic DNA binding dye, EvaGreen (Bio-Rad Laboratories Inc., Hercules, CA).

Multiple inter-run calibrators were always used to allow comparison of Ct values obtained in different runs. The primers for both housekeeping and target genes were designed with a specific software Beacon Designer® (version 8.1; Premier Biosoft International, Palo Alto, CA) with reference to nucleotide sequences included in the NCBI database GenBank (http://www.ncbi.nlm.nih.gov/Genbank/index.html) (Table S3) and synthesized by Sigma-Aldrich (Milan, Italy). Moreover, to provide greater transparency of our results between research laboratories, this study was carried out to conform to the Minimum Information for Publication of Quantitative Real-Time PCR Experiments [54]. Relative quantification of each target gene studied for the molecular analysis of explants was calculated by the $2^{-\Delta\Delta Ct}$ method with dedicated software (CFX Manager Software Bio-Rad). When expression values were not normally distributed, the logarithmic transformation of data was used for statistical analysis.

2.3.5. Histology, immunohistochemistry and immunofluorescence examination

The heart sections were deparaffinized in xylene, rehydrated in an ethanol series and then processed for either histological or immunofluorescence experiments. Some sections were stained with either haematoxylin and eosin (H&E) or Ionized calcium-binding adaptor molecule 1 (anti-Iba1, 1:1000; 019–19741, Wako Chemicals USA) to evaluate cardiac tissue morphology and inflammatory infiltration. In parallel, Masson and Mallory's Trichrome (MT) staining for fibrosis and foreign body reaction assessment were performed on other sections. Slides were dehydrated in ethanol series, cleared with xylene and cover-slipped with Permount. Stained sections were analyzed using light microscopy (Olympus, Tokyo, Japan) at 10–40X magnifications and equipped with a digital RGB video camera (Olympus DP 20, Tokyo, Japan) to capture the digital format of images. For anti-Iba1, antigen retrieval was performed with Discovery CC2 (Ventana Medical Systems Inc.) at 98 °C for 80 min. Slides were incubated with the primary antibody for 1 h RT, then detection was performed with Discovery Omnimap anti-rabbit HRP and ChromoMap-DAB (Ventana Medical Systems Inc.).

For immunofluorescent analysis, after deparaffinization and rehydration, permeabilization in 0.15 % Triton X-100 and blocking of non-specific binding sites incubating samples with 6 % BSA and 3 % NGS were performed. Tissue sections were then incubated with primary antibodies directed against anti-TnC (1:30, sc-48347, Santa Cruz, Germany), anti-Cx43 (1:100, C6219, Sigma-Aldrich, Milan, Italy), anti-smooth muscle α-actin (α-SMA) (1:50, ab5694, Abcam, Cambridge, UK), anti-von Willebrand factor (vWF) (1:50, 27186-1-AP, Proteintech, Manchester, UK), anti-c-Kit (1:50, 18696-1-AP, Proteintech, Manchester, UK), anti-GATA-4 (1:50, bs-1778R, Bioss, Woburn, USA), anti-CD68 (1:100, MA5-13324, Invitrogen, Thermo Fisher, Monza, Italy) anti-CD80 (1:100, PA5-79001, Invitrogen, Thermo Fisher, Monza, Italy) and anti-CD163 (1:100, MA516658, Invitrogen, Thermo Fisher, Monza, Italy) O/N at 4 °C, and with secondary antibodies conjugated to phycoerythrin (1:200, sc-3738, Santa Cruz, Heidelberg, Germany), Alexa Fluor 488 (1:200, A11070, Invitrogen, Thermo Fisher, Monza, Italy or 1:200, IS-20246, Immunological Sciences, Rome, Italy) or Alexa Fluor 647 (1:200, A21242, Invitrogen, Thermo Fisher, Monza, Italy) for 2 h at RT. Samples were then washed in PBS, and total nuclei were counterstained using DAPI (1:2500, Sigma-Aldrich, Milan, Italy) nuclear dye for 30 min. Samples were stored at 4 °C in the dark and imaged using a laser scanning confocal microscope (LSM510, Carl Zeiss, Oberkochen, Germany).

For TnC and Cx43 assessment, the quantification of fluorescent signals was performed in three fields for each slice (1 slice for each animal). The fields were acquired in the subepicardial region of the left ventricle for all groups, in particular under the patch for the I/R + P and Sham + P groups, or in the infarcted area for the I/R group. The images were acquired with the Z-stack option (10 slices at 10X, z-spacing of 40.5 μm, 16 bit, 1024 × 1024 resolution). The intensity of fluorescence was measured with ZEN 2.5 blue edition software (Carl Zeiss Microscopy GmbH, Oberkochen, Germany) and normalized with DAPI [55]. For blood vessel quantification five fields for each slice were captured at 10X in the left ventricle as previously indicated. Tubular structures positive for α-SMA staining, identified as vessels, were counted and classified based on their size. The vessels were also quantified in the patch with the same method. The quantification was expressed as the number of vessels per mm^2. vWF fluorescent signal was used for capillary quantification [7] and fluorescence intensity was quantified.

The assessment of GATA-4 and c-Kit positive cells was carried out in three fields, for each slide, captured at 63X. The quantification was expressed as the number of positive cells per mm^2.

For the estimation of the inflammatory response in cardiac tissue, 40X magnification pictures of H&E staining were captured and the following scoring system was applied: 0 = Absent; 1 = 1 to 5/high power field (hpf); 2 = 5 to 10/hpf; 3 = Mild infiltrate; 4 = Moderate infiltrate; 5 = Heavy infiltrate. On other slices, total macrophage infiltration was evaluated with 40X magnification pictures of cardiac tissue stained with anti-Iba1 and the following scoring system was applied:=absent; + = 1 to 5/hpf; ++ = 5 to 15/hpf; +++ > 15/hpf.

For macrophage polarization evaluation, a double staining with anti-CD68 and anti-CD80 was performed to identify the pro-inflammatory (M1) phenotype, while a double staining with anti-CD68 and anti-CD163 allowed the identification of the anti-inflammatory (M2) phenotype. Quantification was carried out in three fields, for each slide, captured at 40X magnification. Macrophage polarization was expressed as M1/M2 ratio.

2.4. Statistical analysis

For patch characterization (mechanical and rebinding tests) was performed, statistical analysis using two-way parametric ANOVA, followed by Tukey's HSD post-hoc tests. Statistical analysis for DLS data through One-Way ANOVA (Welch correction) was performed, with the Dunnett post-hoc test.

For *in vitro* cell and ex-vivo cardiac sample analyses, Student's t-tests or one/two-way parametric ANOVA followed by Tukey's HSD post-hoc tests were used.

For Calcium Imaging analysis, when data residuals did not exhibit significant deviations from normality (Shapiro–Wilk test) or heteroscedasticity (Levene's test), two-independent-samples t-tests or one/two-way parametric ANOVA followed by Tukey's HSD post-hoc tests were used to assess the statistical significance of the effect (i.e., the difference between group means). On the contrary, when those assumptions did not hold, non-parametric alternatives (i.e., Mann–Whitney *U* test or Kruskal–Wallis H test followed by Dunn's post-hoc test) were preferred to compare groups.

For *in vivo* gene expression, the differences between the four independent groups were analyzed by Fisher's test after ANOVA. All data were analyzed by using Statview 5.0.1 software released for Windows Statistical (SAS Institute, Inc., Cary, NC, USA). For FT-IR Chemical Imaging results, Principal Component Analysis (PCA) was performed to analyze the large spectral data sets.

In any case, an effect was considered statistically significant for (adjusted) p-values <0.05 ($^*p < 0.05$; $^{**}p < 0.01$; $^{***}p < 0.001$). Depending on the context, data were represented as mean ± standard error of the mean (SEM) in the form of bar charts, or as median and interquartile range (IQR) in the form of box plots, as specified in the caption of each figure.

3. Results

3.1. Production and physico-chemical, morphological, mechanical and functional characterization of MENDEP

MENDEP (Fig. 1) consists of two microstructured bioartificial polymeric interfaces based on PLGA, Gelatin and Fmoc-FF, integrated with an intermediate layer of Fmoc-FF based-hydrogel loaded with Apelin-13. Two classes of nanoparticles (NPs) based on PVP-PMAA MIPs towards MMP-9 and poly-3-hydroxybutyrate (PHB) NPs containing Apelin-13 were produced and sprayed at two different densities onto external microstructured surfaces. MIP towards MMP-9 were characterized using various analyses including SEM, Thermogravimetric analysis (TGA) and HPLC. PHB NPs loaded with Apelin-13 were analyzed by SEM, DSC, TGA, FT-IR Chemical Imaging and HPLC. PHB NPs were evaluated for their capability of releasing Apelin-13 in effective doses, as a stem cell recruitment factor, cardioprotective drug and neo-vascularization enhancer in the peri-infarct area.

A wide series of characterizations were performed on MENDEP: physico-chemical (FT-IR Chemical Imaging, DSC, TGA) mechanical (DMA, INSTRON), degradation (weight loss, GPC) and functional analyses (HPLC). Moreover, a conductivity analysis was carried out to verify the contribution of the peptide Fmoc-FF to the electroconductivity of the patch, using an impedance spectrometer.

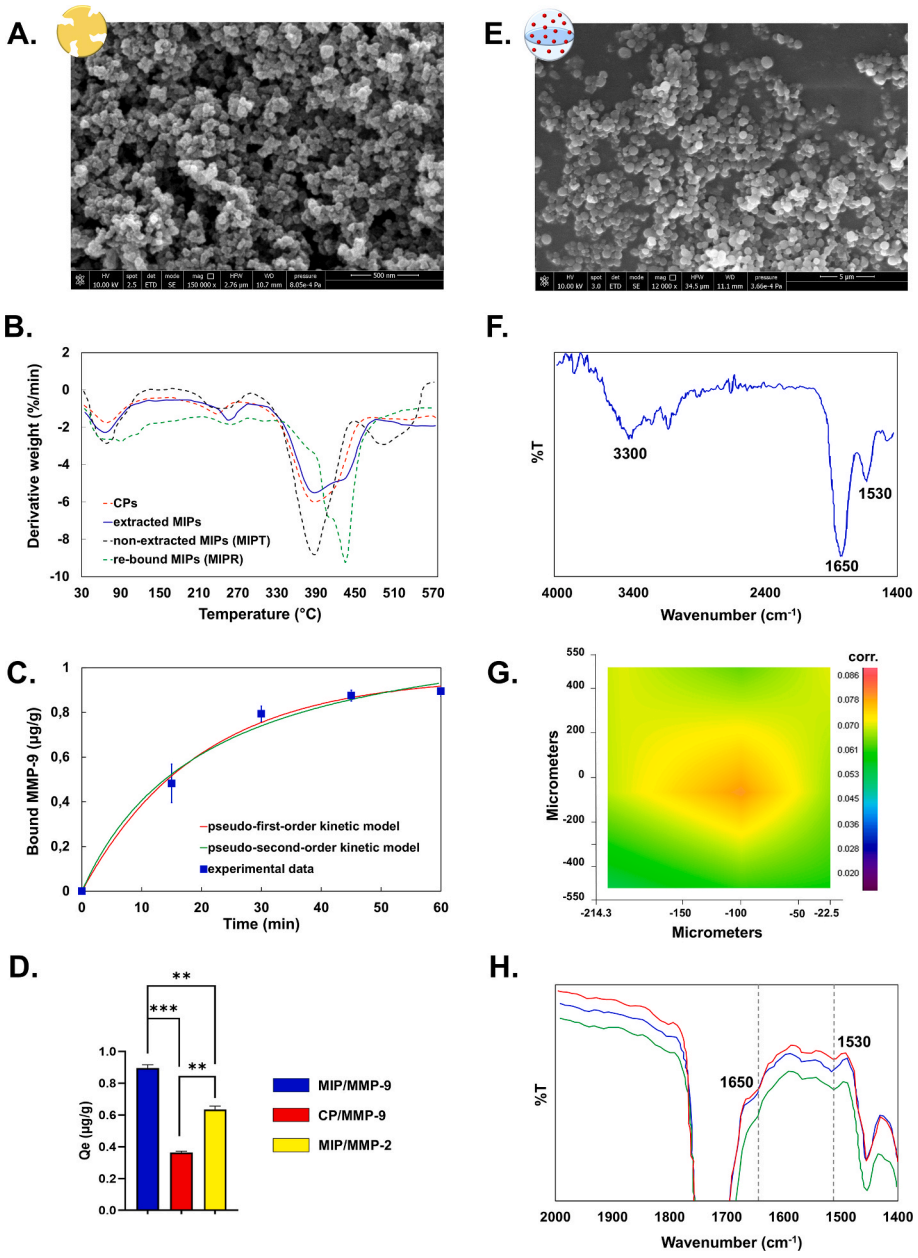

Fig. 2. Physico-chemical and morphological characterization of MMP-9-MIP and PHB NPs loaded with Apelin-13. A. SEM image of MIP aggregates after hMMP-9 extraction. **B.** The first derivative of thermogravimetric curves corresponds to CPs (red), extracted MIPs (MIP, blue), non-extracted MIPs (MIPT, black) and re-bound MIPs (MIPR, green). **C.** Fitting of the experimental data for rebinding curve of MMP-9 towards MIPs using pseudo-first-order model (blue) and pseudo-second-order model (green) (n = 6). **D.** Qe for MIP/MMP-9 (blue), CP/MMP-9 (red), and MIP/MMP-2 (yellow). ***p < 0.001, **p < 0.01, by two-way ANOVA with Tukey's post-hoc tests (n = 6). **E.** SEM image of PHB NPs loaded with Apelin-13 aggregates. **F.** FT-IR Chemical Imaging: identification of the typical bands of the average spectrum on Apelin-13 PHB NPs. **G.** Correlation map of Apelin-13 with respect to Apelin-13 PHB NPs **H.** Magnification of spectra acquired on a layer of NPs showing Apelin-13 bands in the range 1700–1500 cm^{-1}.

3.1.1. Molecularly imprinted nanoparticles vs MMP-9

NPs imprinted towards MMP-9 were prepared using a radical polymerization by precipitation method in monomer (MAA) dilute solution and in the presence of PVP. The choice of using PVP is due to its hydrophilic properties, its approval by FDA for many uses and its similar structure to protein, for an expected better tissue interaction. MIP NPs were prepared in the presence of MMP-9 following three steps according to the paradigm MIP synthesis: 1) Non-covalent molecular interaction formation among MAA monomers, pre-formed PVP and MMP-9 (T), 2) Initiation and crosslinking with initiator and cross-linker (MIPT), 3) T extraction with the production of MIPs. The same steps were performed for control NPs (CP) with the only difference of MMP-9 absence.

The residual MMP-9 was analyzed via HPLC. The percentage of MMP-9 at the end of the polymerization and after the extraction phase were respectively 95.2 % and 67.2 %.

3.1.1.1. Dimensional and morphological analysis. DLS analysis showed aggregates in phosphate-buffered saline (PBS) of MIP (747 ± 17 nm) after extraction revealing a significant reduction of the size (p-value ≤ 0.05) compared to MIPT (diameter 2144 ± 608 nm). This is due to the removal of both the enzyme aggregates and unbound PVP. Comparing MIP after the extraction and CP, we can see that CP is significantly bigger (1023 ± 140 nm; p-value ≤ 0.05) than the MIP diameter. SEM analysis was performed to distinguish single NPs from aggregates and obtain a more specific size comparison. The difference in diameter between CP (351 ± 27 nm) and MIP (310 ± 53 nm) (Fig. 2A) was not significant, indicating that the enzyme does not hinder the polymerization process during the MIP formation.

3.1.1.2. Thermal analysis. In Fig. 2B the first derivative of the thermogravimetric curves obtained for CP, MIPT, MIP and MIPR (MIP after MMP-9 rebinding) showed three important events: the first one, between 30 and 100 °C, due to the loss of water present in the samples; the second one, between 200 and 300 °C, due to the formation of anhydrides between the acrylic components; the third one, between 300 and 500 °C, attributable to the complete degradation of the polymeric chains of the PVP-PMAA complex. In Table S3, the calorimetric data obtained by analyzing the derivative curves are reported. There was no significant variation in the maximum rate of degradation related to the second degradation event (200–300 °C), while an increase in the percentage of weight loss in samples containing the enzyme (MIPT and MIPR) compared with those that do not contain (CP) or minimally contain (MIP) the enzyme.

The data relating to the third degradation event (300–500 °C) show an increase in weight loss in the samples containing the enzyme as well. In addition, a shift towards higher temperature values corresponding to the maximum degradation rate can be noted, which could be due to higher stabilization of the PVP-PMAA complex into the nanoparticle matrix induced by the presence of the enzyme molecules.

3.1.1.3. Molecular recognition and selectivity tests. HPLC was used to study PVP-PMAA MIP rebinding capacity with respect to the enzyme MMP-9. The selectivity of the nanoparticles was also demonstrated through a comparison with the rebinding ability towards MMP-2, an analogue enzyme.

The kinetics of rebinding of MMP-9 to MIP are reported in Fig. 2C. Q_t is the quantity of enzyme bound (in μg), by 1 g of particles at a certain time *t*. In the initial stage, the amount of enzyme linked to the MIP increases rapidly, as the number of unoccupied cavities is high and the MMP-9 can easily occupy the free sites, leading to rapid adsorption of the template. After 30 min, the amount of MMP-9 that binds to MIP increases more slowly, due to the cavities that begin to saturate in the NPs, and a plateau is reached after 1 h. The control particles are also able to bind to the enzyme. This is due to the presence of randomly distributed functional groups in the polymeric matrix, responsible for non-specific adsorption. The analysis of CP allows the discrimination of the quantity of enzyme bound in a non-specific way from that bound by the specific sites due to molecular imprinting. The equilibrium value Q_e expresses the enzyme (in μg) linked to 1 g of NPs at the equilibrium. After 60 min, both MIP and CP reached the Q_e values of 0.89 ± 0.02 μg g^{-1} and 0.36 ± 0.04 μg g^{-1}, respectively. The recognition factor (i.e., the ratio between Q_e of MIP and that of CP) is equal to 2.45, showing that the capacity of MIP to bind the enzyme is greater than that of CP, thanks to the formation of specific recognition sites.

Moreover, selectivity was evaluated by measuring the capacity of MIP to bind the MMP-2 enzyme. A comparison between the three Q_e values measured for MMP-9 rebound by MIP or CP and for MMP-2 by MIP was performed (Fig. 2D). The Q_e of MMP-2 rebound by MIP has a lower value compared to Q_e of MMP-9 rebound by MIP, confirming a good selectivity. Moreover, the Q_e of MMP-2 is higher (0.63 μg g^{-1}) than that of MMP-9 by CP. This is because MIP cavities also bind the MMP-2 enzyme which is very similar to MMP-9, both in terms of size and functionality.

Different models were developed based on which step is assumed as the lowest, namely the one which limits the rate of process [56]. The kinetic models of pseudo-first and pseudo-second order assume that the limiting phenomenon is the adsorption reaction of the adsorbate (enzyme) on the adsorbent (nanoparticle) [51].

The experimental data and the two fitting curves, the pseudo-first-order model (red) and pseudo-second-order model (green) are shown in Fig. 2C.

An optimization process allowed us to determine the unknown parameters (Q_{e1}, k_1) for the first-order model and (Q_{e2}, k_2) for the second-order model. These parameters are those that allow us to obtain the best fitting of the experimental data: (Q_{e1}, k_1) = (0.96, 0.05) (Q_{e2}, k_2) = (1.26, 0.038). To establish which of the two models allowed a better fitting of the data, the square of the residuals was calculated and obtained as the sum of the quadratic differences between the values determined by the kinetic model and the experimental ones.

For the pseudo-first-order kinetic model, the residual square is 0.0032, while for the second-order model, it is 0.0063. It follows that the pseudo-first-order model allows to better describe the experimental data than that of the second order. Furthermore, Q_e obtained from the first-order kinetic model is closer to that obtained experimentally (0.89).

3.1.2. PHB NPs releasing Apelin-13

PHB NPs loaded with Apelin-13 were produced and characterized by SEM, DLS, FT-IR Chemical Imaging, DSC and HPLC.

3.1.2.1. Dimensional and morphological analysis. SEM analysis performed on PHB NPs confirmed the production of PHB particles by precipitation method. The morphological properties of PHB particles before and after Apelin-13 loading (Fig. 2E) pointed out a spherical shape, a smooth surface, a good dimensional homogeneity, and a certain degree of aggregation after drug loading.

The comparison between SEM images of PHB nanoparticles before and after Apelin-13 loading showed an increase in size after absorption of Apelin-13, in agreement with DLS results (data not reported). However, the size of NPs remains below 1 μm also after loading.

3.1.2.2. -IR chemical imaging, thermal analysis. The physico-chemical characterization of pure PHB, PHB NPs, pure Apelin-13 and PHB NPs loaded with Apelin-13 was performed using FT-IR Chemical Imaging.

The acquisition of IR spectra for pure PHB and PHB NPs highlights that there are no differences between the two samples. This indicates that, during the preparation of particles, substances that could alter the chemical structure of the pure material are not left in the final product. An aliquot of PHB NPs loaded with Apelin-13 was directly analyzed by FT-IR Chemical Imaging. Spectra were acquired by chemical mapping confirming the effective Apelin-13 adsorption at 3330 cm^{-1} (amino

group), 1650 cm^{-1} (Amide I) and 1530 cm^{-1} (Amide II) (Fig. 2F). The correlation map of drug with respect to loaded PHB NPs is reported in Fig. 2G. Magnification of the associated spectra shows a small shoulder at 1650 cm^{-1}, associated with Amide I and at 1530 cm^{-1} of Amide II corresponding to the presence of Apelin-13 in the particle aggregates (Fig. 2H).

To evaluate the purity of samples as well as the crystallinity amount, DSC analysis was carried out. The calorimetric analysis (DSC) allowed us to obtain the thermogram of raw PHB ($T_m = 174$ °C, $\Delta H = 70$ J g^{-1}), pure PHB NPs ($T_m = 172$ °C, $\Delta H = 45$ J g^{-1}) and PHB NPs loaded with Apelin ($T_m = 168$ °C, $\Delta H = 11$ J g^{-1}). The thermograms show a single endothermic degradation event (melting temperature) for all samples. The T_m value decreases slightly after Apelin loading, but not significantly. The curves do not show the glass transition event, because the T_g for PHB is less than 10 °C. Instead, a significant variation of enthalpy is evident during the melting process, which could be associated with a different crystallinity of the samples, particularly evident after drug loading.

A further evaluation was performed by TGA (data not shown). An important single event of mass loss (200–250 °C) was registered for all three samples, but with a strong shift towards higher temperatures moving from PHB NPs with Apelin-13, PHB NPs and PHB pure, confirming the significant variation of enthalpy observed by DSC analysis.

3.1.2.3. Drug loading and release from PHB NPs. The drug loading efficiency was 80 %, determined by calculating the percentage of Apelin-13 absorbed by PHB NPs (after reaching equilibrium at 2 h of incubation) respect to the initial amount of Apelin-13. The analysis of Apelin-13's release from PHB NPs showed a sustained and prolonged drug release when monitored at different time intervals, with a rapid release in the first 2 h, followed by a continuous and gradual release up to 72 h (Fig. 3L, upper panel). This result agrees with the usefulness of Apelin-13 to give a cardioprotective effect in the early hours, to act as a recruitment factor of stem cells and induce vascularization over time, thus maintaining its cardioprotective effect on the myocardium after reperfusion [30,36,39].

3.1.3. Characterization of MENDEP

3.1.3.1. Conductivity test. Conductivity analysis was carried out to study the conductive properties of the patch, using an impedance spectrometer (Fig. S4). For the analysis, the sample was inserted in a Teflon ring and covered by two metallic plates, to contain the swelling of the cardiac patch and maintain constant the thickness of the sample during the test. Previous observation showed that 70 % of swelling within the double distilled water at 37 °C occurs in 30 min, then a quite stable behavior was observed. The conductivity values obtained for different samples of MENDEP analyzed after 30 min of swelling were reported in Fig. 3A, showing values of about $6.0 \cdot 10^{-5}$ S/cm at 1 Hz.

A comparison between the conductivity trend for patches with and without Fmoc-FF was made, the lower values ($4.6 \cdot 10^{-5}$ S/cm at 1 Hz) obtained for patch in the absence of peptide (MNDEP) confirms the effect of Fmoc-FF to increase the electrical conductivity of the PLGA/Gelatin-based patch.

To evaluate the effect of incorporation of Gelatin into PLGA membrane, the conductivity values vs frequency for m-PLGA ($8.0 \cdot 10^{-7}$ S/cm at 1 Hz) and m-MP ($5.5 \cdot 10^{-6}$ S/cm at 1 Hz) were measured and reported in Fig. 3A. Comparing the values, it is evident how the pure PLGA shows the highest impedance and the introduction of Gelatin favors an increase of electrical conductivity if compared with m-PLGA. However, m-MP settled on lower values than both bilayer samples (MNDEP and MENDEP), regardless of the presence of Fmoc-FF.

3.1.3.2. Dynamic mechanical analysis. Dynamic mechanical analysis (DMA) was carried out on MENDEP along transversal and longitudinal directions with respect to surface micropatterning. Fig. 3B and C showed the storage and loss modulus and the tanδ damping factor as a function of the stress frequency, for samples tested in the longitudinal and transversal direction, respectively. As visible from the plots, both loss and storage modulus increase almost linearly as the frequency increases ($R2 \geq 0.96$). However, from the statistical analysis, there is no significant variation of the modulus with increasing frequency. The damping factor remains almost constant, indicating that the storage and loss modulus increase by the same amount as the frequency increases. These trends are similar to those found in the literature for DMA analysis on samples of ovine and porcine myocardium [57]. DMA analysis was carried out also on samples after degradation at 4 and 7 days, at an oscillation frequency of 1 Hz. From Fig. 3D and E, along with the increase in degradation time, there is a decrease in the storage and loss modulus, while the damping factor remains almost constant (0.52 ± 0.17). The degraded samples tested in the longitudinal direction, as well as those at time 0, show a significant difference between the loss and storage modulus, indicating that the elastic behavior continues to be predominant even after 7 days of degradation. Fig. 3F highlighted that the mechanical anisotropy of the patches is present and continues to reflect the topographical one, even if a significant difference did not emerge at 7 days.

3.1.3.3. Hydrolytic degradation. The hydrolytic degradation of each sample was evaluated both by weight loss over time and by change of the weight average (Mw) and numeral (Mn) molecular weight over time. Weight loss during hydrolytic degradation is caused by the formation of water-soluble low molecular weight monomers and oligomers following the breakdown of the polymer chains and their subsequent release into the aqueous medium [58]. From Fig. 3G, it is possible to observe a slow decrease in weight over time, which reaches just 15 % after 30 days of degradation. Mw and Mn profiles show a similar trend: at 7 days there is a first strong variation and, after 30 days, a drop of around 35 % is reached compared to the initial values (Fig. 3H and I).

These results seem to be consistent with the mechanical results where the degradation at 7 days caused a reduction in the mechanical behavior, although still measurable, while at longer times the effect of the degradation produced a substantial change in the patch, which did not allow mechanical measurements.

The results suggest a bulk-type degradation, which can essentially be divided into two stages. Initially, a significant decrease in molecular weight occurs without substantial weight loss; subsequently, significant weight loss occurs accompanied by a decrease in molecular weight [58]. This degradation kinetics is consistent with the degradation of PLGA, the most abundant component in the patches, as reported in the literature [59]. Furthermore, the slow degradation of the patch allows efficient support for tissue regeneration even at longer times, since the integrity of the microstructured profiles during the *in vitro* incubation period is perfectly maintained for up to 30 days.

3.1.3.4. Suture test. Suture resistance tests are commonly performed on patches and tubular prostheses, as their implantation in the site of interest requires a suture operation.

A tensile test was performed using INSTRON following the ISO 7198:2017 which relates to cardiovascular implants, such as vascular prostheses, tubular vascular grafts and vascular patches.

The suture point was inserted 2 mm from the end of the patch (Fig. S1A). The suture was held by the upper clamp and a uniaxial tensile test was performed with a load cell of 100 N (Figs. S1B and C). According to the ISO standard, the speed test was set at 50 mm min^{-1}.

Rectangular samples were tested in the longitudinal and transversal direction, both in dry and wet conditions. Wet conditions were obtained by immersing the samples in PBS for 20 min. This test determines the maximum suture force that could break the patch.

The minimum suture force was calculated as follows: $F = \sigma_w \times h \times d_s$,

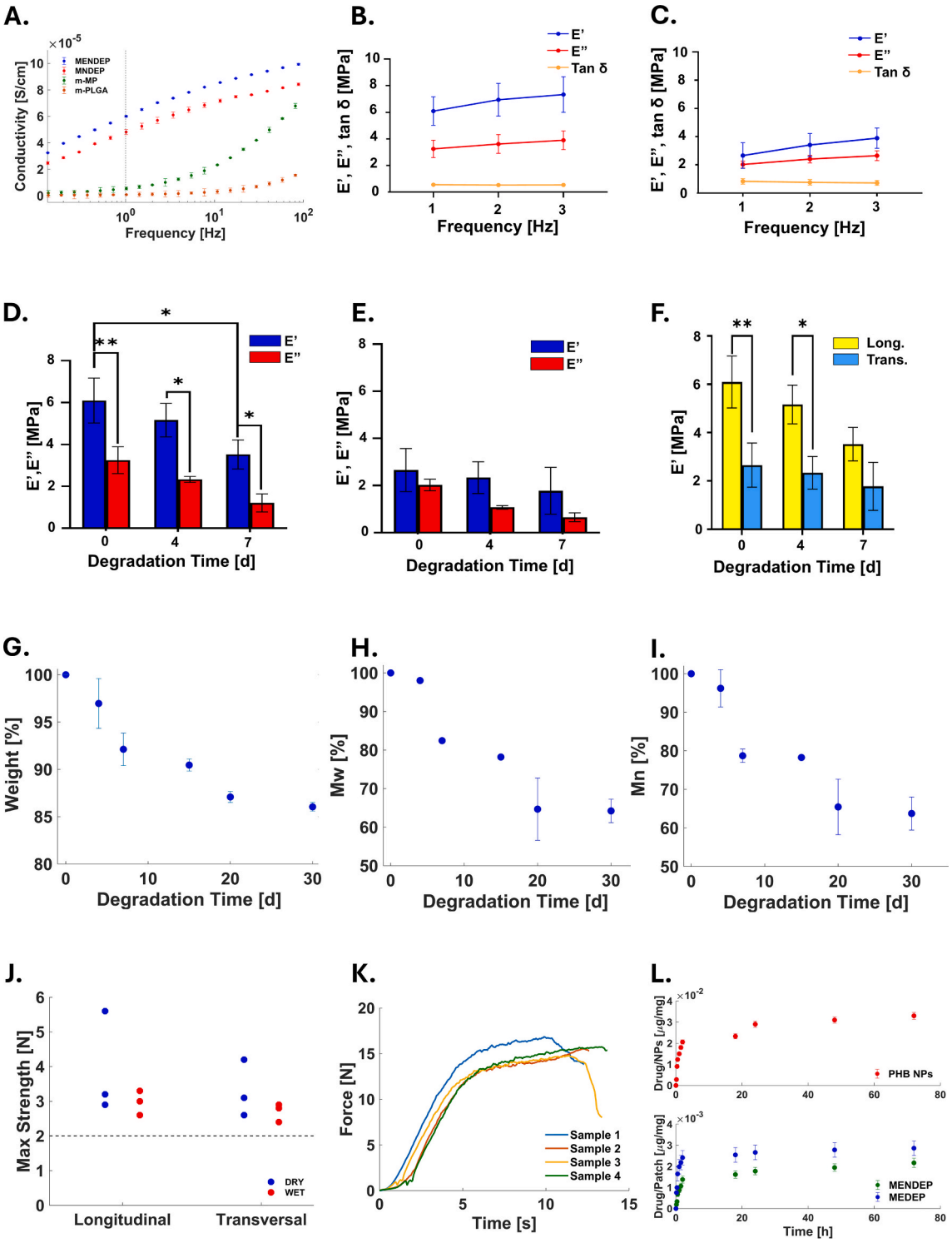

Fig. 3. MENDEP characterization: conductivity, mechanical and degradation tests, suture, burst strength and release tests. A. Comparison between the conductivity of MENDEP (in blue), patch without Fmoc-FF (MNDEP, in red), single membrane of PLGA/Gelatin (m-MP, in green), single membrane of PLGA (m-PLGA, in orange), as function of frequency, under wet conditions (n = 3). Gray line is traced at a stress frequency of 1 Hz. **B.** Storage (blue) and loss (red) modules and Tanδ (orange) damping factor as a function of the stress frequency, for samples tested at time 0 in the longitudinal direction,and **C.** in the transversal direction (n = 6). **D.** DMA results on tested samples at different degradation times along longitudinal, and **E.** along transversal direction (n = 6). Only the significant differences are reported, *p ≤ 0.05, **p ≤ 0.01, by two-way ANOVA with Tukey's post-hoc tests. **F.** Testing direction effect on the storage modulus of samples at different degradation times *p ≤ 0.05, **p ≤ 0.01, by two-way ANOVA with Tukey's post-hoc tests. **G.** Degradation rate in terms of weight loss (%) vs time (n = 3) **H.** Trend of weight molecular weight average (Mw) vs degradation time (n = 3). **I.** Trend of numeral molecular weight average (Mn) vs degradation time (n = 3). **J.** Suture test results for MENDEP, minimum strength specification (2.28 N), traced by a dashed line, two-way ANOVA (n = 6). **K.** Burst resistance force vs time curves for MENDEP samples (n = 4). **L.** Release trends of Apelin-13 from PHB NPs or MEDEP (patch with Apelin-13 inside the hydrogel and without loaded PHB NPs) or MENDEP vs incubation time (n = 6).

where.

- σ_w is the stress on the ventricular wall: 16.1 ± 2.4 kPa. This value corresponds to the stress in the longitudinal direction measured in patients suffering from high LV pressure [60];
- h is the thickness of the ventricular wall: 13.4 ± 2.1 mm. This value corresponds to the thickness of the wall at the end of the systole [61];
- d_s is the distance between one suture and the next one, conventionally 2 mm.

The force per suture is equal to 0.57 N/suture, considering the upper extremes of the intervals including the stress (18.5 kPa) and the thickness (15.5 mm) values.

The ventricular wall was assumed isotropic and homogeneous. This means that the stress on the ventricular wall in the longitudinal direction, also called southern, ($\sigma_{\varphi\varphi}$) was assumed equal to the circumferential one ($\sigma_{\theta\theta}$). Because of the assumptions made, a safety factor equal to 4 was introduced. It follows that the minimum suture force that the patch must resist becomes: $F = 0.57 \times 4 = 2.28$ N/suture.

The patch can be applied to the myocardium via glue and/or suture. Therefore, the assessment of the resistance of the patch to the suture is necessary to validate the safety and efficacy of the device for future implantation in the human heart.

The force-deformation curves of samples tested both in dry and wet conditions are shown in Figs. S1D and E, respectively. The ability of the patches to resist suturing was evaluated by determining the maximum force they could withstand during the tensile test. In Fig. 3J the results of the suture test for all analyzed patches showed a suture strength greater than the calculated minimum strength specification (2.28 N).

The compliance of the samples was also assessed (Fig. S1F). High compliance values indicate that, with the same deformation, greater force is required to stretch the sample under examination. This implies that the polymeric structure offers greater resistance to deformation. The statistical analysis (2-way ANOVA with Tukey's post-hoc test) reports a significant difference in the compliance values of the samples tested dry in the two different directions. This means, once again, that the longitudinal direction is more resistant than the transversal one.

3.1.3.5. Burst strength test. The burst resistance test was performed to simulate the biaxial forces to which the patch is subjected *in vivo* and to determine its resistance when subjected to significant load conditions. The test was performed following the ISO 7198:2017 standard using a testing apparatus designed, according to the example reported into the ISO, using Solidworks 3D CAD software and produced (Figs. S1G and H). The apparatus components obtained were mounted on the INSTRON (Fig. S1I). During the compression test, the probe displacement speed was set to 50 mm min^{-1} and the sampling time every 2 ms. The maximum force recorded in the force-time curves was identified as the resistance burst force. The burst resistance of the patch must be adequate to prevent rupture or bleeding around the patch during the continuous cycles of contraction and relaxation of the heart [62]. Ideally, the patch should possess mechanical properties that allow normal tissue function near the implantation site.

The burst strength test was performed to simulate the biaxial forces to which the patch is subjected *in vivo* and to determine the strength of the patch under relevant physiological loading conditions [58].

In fact, once implanted, the patch is mostly subjected to biaxial rather than uniaxial stress. Therefore, the characterization of the biaxial parameters assumes considerable importance. The results of the bursting strength test are shown in Fig. 3K, showing a value of burst resistance force, the maximum force recorded in the force-deformation curves, equal to 15.72 ± 0.85 N. The strength values obtained are comparable to those determined on porcine LV myocardial samples [63]. The maximum force recorded in the burst resistance tests on myocardial samples was equal to 20.4 ± 6.0 N. It can therefore be deduced that the patch is able to adequately mimic the mechanical behavior of heart tissue under relevant load conditions.

3.1.3.6. Drug release. The release kinetics of Apelin-13 from the MENDEP were evaluated in an aqueous solution at 37 °C under constant stirring. In Fig. 3L (bottom panel) the drug-releasing trend from MENDEP was compared with that obtained from an analogue patch, not modified with NPs and where the Apelin-13 was loaded only in the internal hydrogel layer (MEDEP). The release of Apelin-13 from MEDEP showed a burst effect reaching a plateau at 72 h. On the contrary, the release of the drug from MENDEP showed rapid growth in the first 2 h, then the curve slowed down showing a gradual and controlled release of Apelin-13. For this reason, the release test for MENDEP was prolonged up to 5 days showing a value of $2.3{\cdot}10^{-3}$ μg of drug respect to mg of patch at equilibrium. The release of the drug from MENDEP can thus persist for extended periods, allowing for the multiple functions of this drug, according to the literature data [31–34,39–41,64].

3.2. *In vitro biological analysis of MENDEP*

Several *in vitro* tests were conducted on MENDEP, as schematized in Fig. 5.

3.2.1. *Cytocompatibility and skin sensitizing potential tests*

PHB and hMMP-9-MIP NPs were analyzed for cytocompatibility across a broad range of doses (from 0.64 to 64 μg mL^{-1}) using the PI Flow Cytometry assay and H9C2 cardiomyoblasts, which are a valuable tool for studying cardiac aspects *in vitro*. H9C2 cells were exposed to PHB or MIPs at four different concentrations, and the viability of the cells was evaluated after 24, 48, and 72 h of exposure (Fig. 4A). The analysis demonstrated optimal cell viability at all doses tested. Then, cytocompatibility on MENDEPs was proved with the same approach and time frame using both rat H9C2 cells and hMSCs (Fig. 4B).

In vitro analysis of the skin sensitizing potential of MENDEP was performed through the h-CLAT. According to this analysis, MENDEP did not show any sensitizing potential (Table S6).

3.2.2. *Migration*

According to previous studies, hMSCs are capable of active recruitment at sites of cardiac infarction where they can enhance cell viability, myocardial contractility, and other functions via paracrine signaling activity [64]. In addition, rNMCs represent a heterogeneous population containing fibroblasts, precursors of endothelial cells and, possibly, myocyte cells, that have chemotactic migration ability [65].

A three-dimensional transwell migration assay was performed with these two cell types to assess the chemotactic potential of MENDEP

rNMCs and/or hMSCs were seeded on the top wells of chemotaxis chambers in the presence of 0.5 % FBS and tested for their migration ability towards the lower chamber at different conditions: 0.5 % FBS (negative control), (ii) soluble chemoattractant (Apelin-13, 100 nM), (iii) MEP + MIPs, (iv) MEP + Ape-NPs, (v) MEDEP and (vi) MENDEP. After 24 h, the total number of migrated cells per membrane was determined using ImageJ® software. Interestingly, when the chemotactic efficacy of MENDEP (NP-enriched release of Apelin-13) was compared to MEDEP (hydrogel-mediated release of Apelin-13), it was found that MENDEP was significantly more effective in attracting MSCs (Fig. S7). This result confirms that the long-lasting release of Apelin-13 from PHB NPs enhances patch effectiveness, likely by facilitating the sustained release of Apelin-13, a molecule known for its short half-life [42]. Results from both qualitative and quantitative observations showed that MENDEP was able to maintain the chemotactic behavior elicited by soluble Apelin-13 in rNMCs and even enhanced it in hMSCs (Fig. 4C). This difference in the extent of migration between MSCs and NMCs (5.2- vs 1.5-fold increase, respectively) in response to MENDEP compared to the Apelin-13 solution, is likely attributed to the higher

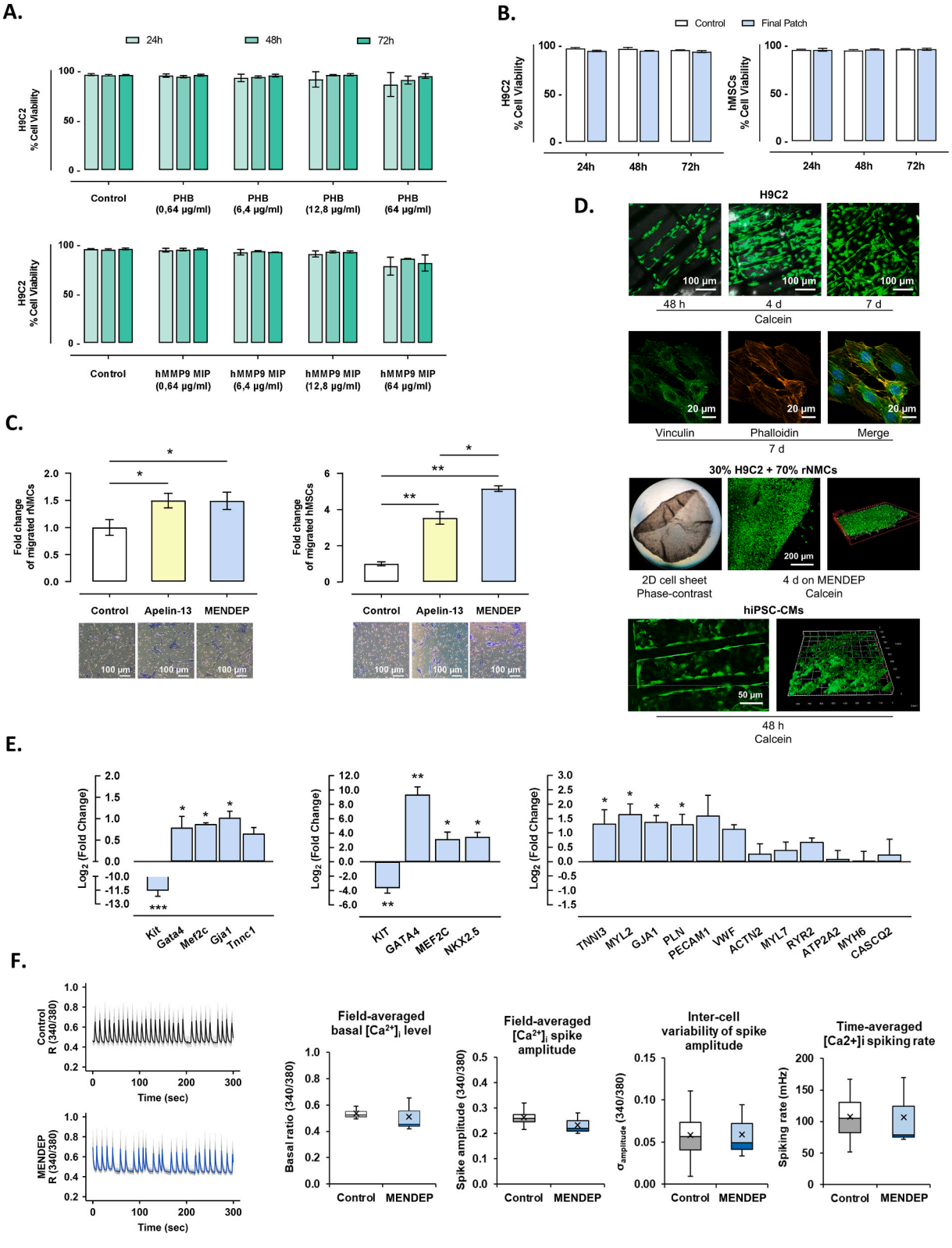

(caption on next page)

Fig. 4. Cellular *in vitro* validation of MENDEP. **A.** Cytocompatibility analyses of PHB and hMMP-9 MIP nanoparticles at different concentrations. H9C2 cells were cultured with nanoparticles at 24, 48 and 72 h (PHB: n = 9; hMMP-9 MIP: n = 6). ns by one-way ANOVA with Tukey's HSD post-hoc tests. Control: cells seeded without nanoparticles. **B.** Biocompatibility of the MENDEP with H9C2 cells and hMSCs at 24, 48 and 72 h (n = 3). Control: cells seeded without scaffold. ns by Student's t-test. **C.** Transwell migration assay with rNMCs (left) and hMSCs (right). The graphs show the fold change of migrated cells toward Apelin-13 and MENDEP (rNMCs: n = 3; hMSCs: n = 2). Images show the migration of rNMCs (left) and hMSCs (right), stained with 0.2 % Crystal Violet. Control: cells migrated toward 0.5 % FBS. *p < 0.05, **p < 0.001, by one-way ANOVA with Tukey's HSD post-hoc tests. **D.** H9C2 cells cultured on MENDEP for 48 h, 4 days and 7 days stained with Calcein-AM (first row) and cytoskeleton structure of H9C2 cells cultured on MENDEP for 7 days, visualized with Vinculin and Tritc-phalloidin staining (second row). Production of a 2D cell sheet composed of NMCs and H9C2 cells (third row, left). Calcein-AM stained cell sheet cultured on MENDEP for 4 days and 3D reconstruction (third row, centre and right). Calcein-AM stained hiPSC-CMs cultured on MENDEP for 48 h and 3D reconstruction (fourth row). **E.** qPCR analyses of stemness and cardiac/vascular differentiation markers in rNMCs (left) or hiPSC-CMs (right) cultured on MENDEP for 7 days (n = 3), and in hMSCs (middle) cultured on MENDEP for 14 days (n = 4). Expression of the same genes in 2D control cultures was used for normalization. The graphs show Log_2 fold changes relative to the RNA expression levels calculated using the $2^{-\Delta\Delta Cq}$ method. *p < 0.05, by Student's t-test. **F.** Traces from single cells are shown transparently in the background; field-averaged signals are shown thicker in the foreground. Right panel: quantitative analyses of intracellular calcium concentration dynamics of hiPSC-CMs cultured with MENDEP and alone (Control, n = 4). The graphs show, from left to right, field-averaged basal $[Ca^{2+}]_i$ level, field-averaged $[Ca^{2+}]_i$ spike amplitude, intercellular variability of spike amplitude, and time-averaged $[Ca^{2+}]_i$ spiking rate.

intrinsic migratory capacity of MSCs. When the MENDEP-induced migration of hMSCs was compared to patches with a single functionalization, the chemotactic efficacy was preserved in the case of MEP + Ape-NPs, whereas it was lost with MEP + MIPs (Fig. S8), confirming that the chemotactic ability of Apelin was responsible for the MENDEP-induced cell migration effect.

3.2.3. Cell growth and alignment

H9C2 cells were cultured on MENDEP and their viability and morphology were observed for at least seven days of culture, using Calcein-AM staining. It is important to note that the cells adopted a stretched morphology and aligned in parallel to each other as they adhered to the patch microstructure (Fig. 4D, first row). Moreover, these cells maintained a proper cytoskeletal organization during MENDEP colonization (Fig. 4D, second row).

As a next step, the cell sheet technology was applied to obtain a 'tissue-like' structure, mimicking the native structure of the myocardium *in vitro*. Since recent works on heart composition reported that cardiomyocytes account for about 30 % only [66,67], cell sheets were obtained using 30 % H9C2 cells mixed with 70 % rNMCs. The cell sheets were cultured on MENDEP and demonstrated their ability to adhere to the scaffold (Fig. 4D middle panel). 3D reconstructions documented the ability of living cell sheets to colonize microstructured scaffold lanes and thickness already at early time points (4 days) (Fig. 4D, third row).

Finally, because of their beating capacity that better mimics human cardiomyocytes [68,69], hiPSC-CMs were employed. By day 1, spontaneous contractions of monolayer hiPSC-CMs were observed on both well plates (data not shown) and MENDEP, and contraction persisted for at least 30 days (Video S9). Moreover, within 48 h from cell seeding, Calcein-AM staining revealed an elongated shape and extensive patch colonization by hiPSC-CMs that follow its microstructure, as also highlighted by 3D reconstruction (Fig. 4D, fourth row).

Taken together, these results demonstrated that H9C2, NMCs and hiPSC-CMs remained viable on MENDEP. In addition, the cells acquired an elongated and stretched shape similar to the 3D cell arrangement in the myocardium. Therefore, we next focused on examining MENDEP's potential to induce cell differentiation.

3.2.4. Cardioinductivity

To evaluate whether 7-day or 14-day culture on MENDEP affected gene expression in rNMCs, hMSCs and hiPSC-CMs compared to 2D control cultures, qPCR was conducted for selected genes involved in cardiomyogenesis and angiogenesis. After being grown on microstructured scaffolds for 7 days, rNMCs demonstrated a decrease in stemness gene expression (relative Kit expression level, -ΔΔCt, corresponding to −11.55 ± 0.617). In addition, there was an increase in the expression of early cardiac transcription factors Gata4 (-ΔΔCt 0.79 ± 0.26) and myocyte enhancer factor 2C (Mef2c) (-ΔΔCt 0.87 ± 0.03), as well as upregulation of the late cardiac gene Troponin C 1 (Tnnc1) (-ΔΔCt 0.65 ± 0.14) and Gap junction protein alpha 1(Gja1) (-ΔΔCt 1.02 ± 0.15) (Fig. 4E, left panel). Basally, hMSCs express c-Kit, a stemness phenotype-related gene (Fig. S10). When cultured on MENDEP for 14 days these cells showed significant downregulation of c-Kit (-ΔΔCt −3.68 ± 0.68) with concurrent increased expression of GATA4 (-ΔΔCt 9.36 ± 1.06), MEF2C (-ΔΔCt 3.15 ± 0.98) and NKX2.5(-ΔΔCt 3.47 ± 0.62) compared to 2D control. Lastly, hiPSC-CMs cultured on MENDEP for 7 days showed a significant enhancement in the expression of genes associated with cardiac function, such as sarcomeric structure, excitation-contraction coupling, and angiogenesis. This suggests that the maturation process of the hiPSC-CMs augmented over time on MENDEP (Fig. 4E, right panel). Specifically, the expression of cardiac Troponin I3 (TNNI3) (-ΔΔCt 1.32 ± 0.49), myosin light chain 2 (MYL2) (-ΔΔCt 1.65 ± 0.36), GJA1 (-ΔΔCt 1.39 ± 0.22) and phospholamban (PLN) (-ΔΔCt 1.30 ± 0.35) genes were significantly increased on day 7, as compared to the 2D control. The expression of platelet endothelial cell adhesion molecule (PECAM1) (-ΔΔCt 1.60 ± 0.71) and vWF (-ΔΔCt 1.14 ± 0.14) genes tended to increase, though not in a significant way. Altogether, these results showed the ability of MENDEP to direct initial rNMC and hMSC lineage specification towards cardiomyogenesis and to improve hiPSC-CM electrical and contractile function in the absence of any external stimuli. When the cardioinductivity of MENDEP was compared to patches with a single functionalization, no specific differences emerged, suggesting that the material components (PLGA/Gelatin/Fmoc-FF) were *per se* responsible for the cardioinductive effect, irrespective of the accompanying functionalization (Fig. S11).

3.2.5. Calcium imaging

It has been well established that the electrical activity at the cardiomyocyte membrane is controlled by ion channels and G protein-coupled receptors, often actuated by calcium transients [70]. hiPSC-CMs seeded on MENDEP, or cultured in control conditions, were loaded with the ratiometric calcium indicator Fura-2AM and imaged by fluorescence microscopy to investigate the ionic mechanisms underlying the spontaneous $[Ca^{2+}]_i$ dynamics. For both conditions, at least three independent experiments were performed, acquiring calcium signals for about 15 min, from at least 20 cells per optical field. For each trace, both basal calcium level and calcium transients were then quantified by evaluating the field-averaged $[Ca^{2+}]_i$ baseline and spike amplitudes, along with their respective intercellular variability (Fig. 4F from left to right). In addition, the time-averaged $[Ca^{2+}]_i$ spiking rate was also measured as an estimate of the beating frequency, while no cross-correlation analysis was performed given the perfectly synchronous nature of all the observed oscillations. Notably, none of these parameters, including the average beating rate and wave synchronicity, proved to be significantly different when comparing the hiPSC-CMs seeded on MENDEP with the hiPSC-CMs cultured in control conditions (Fig. 4F), thus confirming scaffold biocompatibility in the absence of any alterations in the physiological contraction-relaxation behavior. Similarly, no differences were found comparing the hiPSC-CMs seeded on MENDEP with those seeded on patches with single functionalization

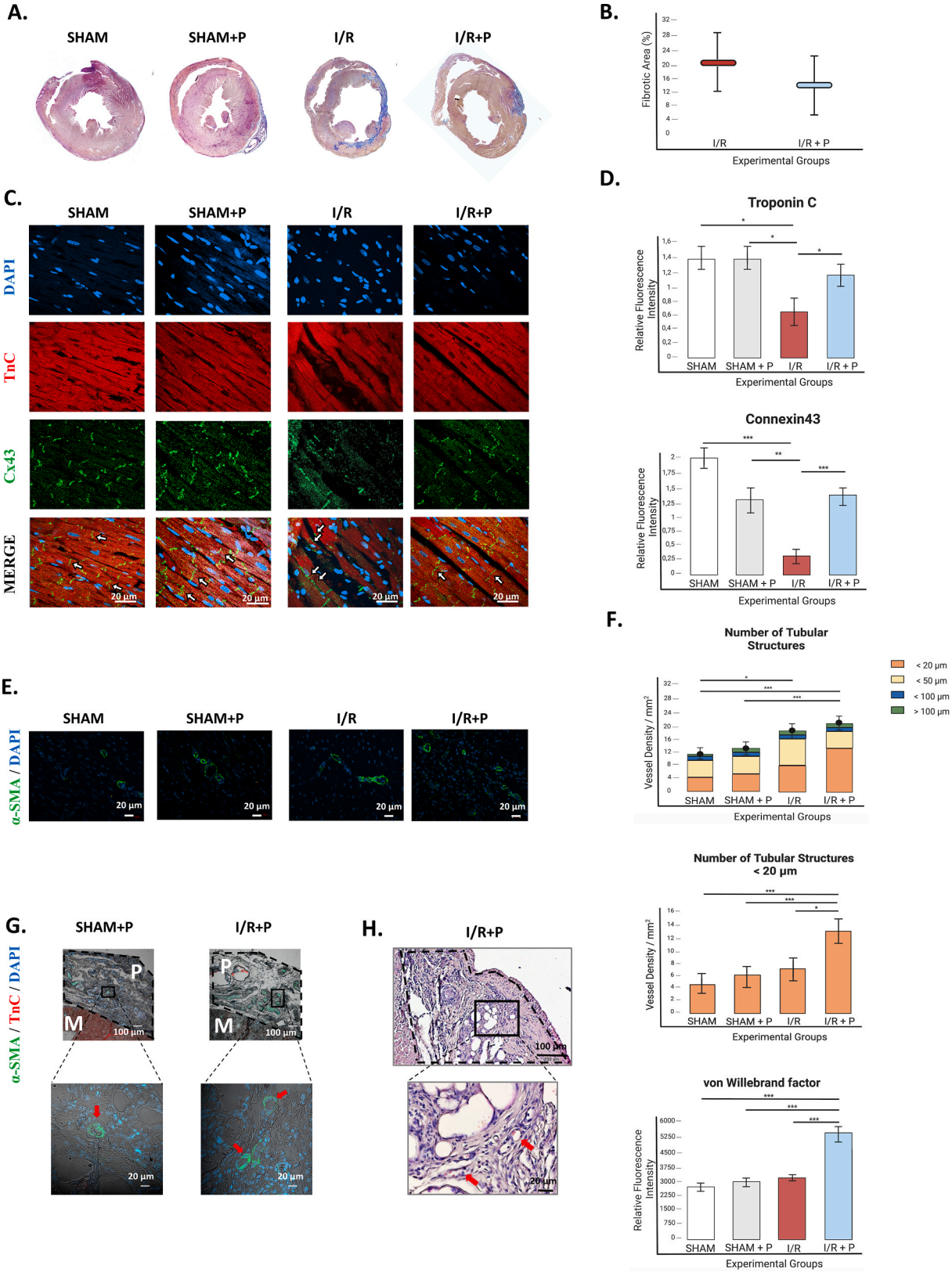

(caption on next page)

Fig. 5. Epicardial MENDEP implantation reduces infarct size and promotes neovascularization in the I/R rat model. A. Representative Mallory's trichrome stained cross-sections of the whole rat hearts for four experimental groups: Sham, Sham + P, I/R, and I/R + P (from left to right). **B.** Histological quantification analysis of interstitial fibrosis in the peri-infarct zone of myocardium in I/R and I/R + P groups (n = 3). **C.** Representative confocal microscopy image depicting low (first row) and high magnification views (from second row on) of immunofluorescent staining on left ventricular sections for each rat group. White arrows point out Cx43 localization in the ventricular tissue. DAPI: blue; TnC: red; Cx43: green. **D.** Quantification of TnC (upper panel) and Cx43 (lower panel) immunofluorescence staining (n = 6). **E.** Representative confocal images showing vessels in the left ventricles of the four groups at low (upper panel) and high (lower panel) magnification. α-SMA: green, DAPI: blue. **F.** Quantification of total α-SMA positive vessels based on their size (upper panel) and vessels less than 20 μm in diameter (middle panel) in five left ventricle regions for each experimental group expressed as Vessel Density per mm^2 (n = 6). Quantification of vWF-positive cells, expressed as fluorescence intensity (lower panel, n = 3). **G.** Representative confocal images of immunofluorescence staining of vessels in the patch implanted in Sham + P and I/R + P rat hearts. Arrows indicate some neovessels formed into the patch at low and high magnification. TnC (red), α-SMA (green), and DAPI (blue). **H.** Representative H&E micrographs showing the patch implanted in an infarcted rat heart (upper panel). Red arrows point to red blood cells showing some functional neovessels at higher magnification (lower panel). M: myocardium; P: patch. *p < 0.05, **p < 0.01, ***p < 0.001, by two-way ANOVA t with Tukey's HSD post-hoc tests.

(Fig. S12).

3.3. In vivo implantation and analysis of heart explants

I/R plays a crucial role in the myocardial damage caused by MI in humans [71]. Indeed, murine models of I/R injury are commonly used to simulate acute or chronic heart disease for cardiovascular research [72]. To evaluate the therapeutic effects of MENDEP implantation, an MI model with I/R injury was utilized in this study. The patches were implanted onto the epicardium of adult Wistar rats and morphological and functional effects were assessed 4 weeks after implantation. The patches (8 mm diameter by 600 μm thickness in size) were entirely positioned over the infarcted area of the rat hearts (Fig. S13).

3.3.1. Post-operative trend

Animals did not show any particular symptoms referring to states of suffering. This is also demonstrated by the fact that their weight gradually increased, reaching values higher than baseline (Figs. S14A–B). There were no significant differences between the average weights of the four groups for the same experimental time.

3.3.2. Electrocardiographic monitoring and magnetic resonance imaging

During surgery, sinus bradycardia was found in T1 (7 cases), T2 (8 cases), T3 (6 cases) and T4 (9 cases), without any difference among the experimental groups, likely due to mechanical ventilation and surgical manipulations.

At T1 (before patch apposition), in 4 rats belonging to the I/R + P group, electrocardiographic signs of ventricular conduction and repolarization disturbance were highlighted, such as electrical alternation of the QRS complex and the T wave, and evidence of single ventricular premature complexes. At T3, electrical alteration of the QRS complex and the T wave, evidence of single atrial and ventricular premature complexes, and ventricular bigeminy were observed in 3 rats belonging to the I/R + P group (data not shown). No changes in the ECG were found at the other time points while the heart rate was normal (Figs. S14C–G). To better assess the *in vivo* conductivity of the MENDEP patch, ECG traces were recorded at multiple time points, allowing a more comprehensive evaluation of its effects on cardiac electrical activity. At T4 (immediately after surgical closure of the thorax), ECG recordings for both the I/R and I/R + P groups showed similar alterations consistent with the acute phase of ischemia/reperfusion (I/R), confirming that the patch does not introduce immediate conduction abnormalities. The evolution of the healing process was further monitored through weekly ECG traces (7d, 14d, 21d, 30d) for both groups. In the I/R group, a persistent QRS complex inversion was observed from 7d onwards, indicative of chronic post-I/R remodeling. In contrast, in the I/R + P group, while QRS complex inversion was initially evident at 7d, a partial recovery was noted over time, suggesting a reduced extent of tissue damage with the implanted patch. Notably, no arrhythmic events or conduction abnormalities were recorded in the I/R + P group at any of the analyzed time points, supporting the safety and functional integration of the MENDEP patch.

A preliminary study using cMRI was also performed on a few animals at 7 and 30 days. The implanted patch in an I/R + P rat was shown to be capable of adequate extensibility such as passive adaptation to the dynamics of the cardiac cycle. Interestingly, LV ejection fraction and stroke volume of the I/R + P animal at 30 days increased (from 55.4 to 74.6 % and from 0.13 to 0.20 mL, respectively), while these parameters decreased in the I/R animal (from 53.4 to 39 % and from 0.09 to 0.06 mL, respectively), thus suggesting positive MENDEP contribution to cardiac contractility (Fig. S15). Moreover, an MRI video of the Sham + P heart showed cardiac mechanical activity after 4 weeks of MENDEP implantation (Video S16).

3.3.3. Histology, immunohistochemistry, immunofluorescence, mRNA expression

After 4 weeks of implantation, optical images showed that MENDEP had a firm adhesion to the epicardium (Figs. S13 and S17). Robust epicardial engraftment of the patches was confirmed by H&E, as illustrated in Fig. S17. The 4-week contact triggered an interaction between the scaffold and the heart tissue. Indeed, the pericardium incorporated the patch into a continuum (Fig. S17). Moreover, the space between the patch and the myocardium resulted in a new deposition of ECM (Fig. S18A). In addition, 4 weeks after MI the patch presented cellular elements (Fig. S18B and see below).

Based on histological analysis in the Sham + P group no evidence of damage was observed in the myocardial tissue beneath the center of the patch, where the single stitch was placed (Figs. S19A and B), apart from a minimal lesion found in one animal (Figure S19C, D and E).

The potential foreign body reactions were also evaluated. Apart from one exception (1 out of 14 animals) where a dense fibrous layer on the outer side of the patch was observed (Figs. S20C and D), Masson's trichrome staining always evidenced a thin layer of loose and vascularized connective tissue (Figs. S20A and B) at the patch-cardiac tissue interface. In addition, in the few animals where the patch was removed after heart explant, MENDEP did not appear to be a rigid or compact structure, nor did it exhibit any concerning thickness. Moreover, the patch was free of microcalcifications.

The total inflammatory infiltrate (both lymphocytes and macrophages) evaluated in H&E sections was scored as rare in both Sham and Sham + P groups, indicating that MENDEP did not elicit any evident immune response *in vivo* (Table S21). The infiltrate was scored as mild in the I/R + P and moderate in the I/R groups, respectively, suggesting MI as the major inflammation cause (Table S21).

The total macrophage analysis based on Iba1 IHC staining was comparably low in the Sham and Sham + P groups, confirming that MENDEP implant does not favor macrophage infiltration (Table S21 and Fig. S22A). After I/R, the total macrophage score increased, irrespective of the presence of the patch (Table S21 and Fig. S22A). The M1/M2 polarization analysis conducted with anti-CD68 (pan-macrophage marker), anti-CD80 (M1 macrophage marker) and anti-CD163 (M2 macrophage marker) antibodies showed in I/R hearts an imbalance of macrophage polarization at the infarct area, with a predominance of M1 pro-inflammatory phenotype over M2 anti-inflammatory phenotype (Figs. S22B and C). At variance, the M1/M2 ratio was completely balanced in the I/R + P group (Figs. S22B and C). These findings suggest

that MENDEP supports favorable immune modulation minimizing pro-inflammatory reactions.

Mallory's staining analysis of infarcted hearts showed that the fibrotic areas in the I/R + P group (14.6 %) were smaller than in the I/R group (20.6 %), suggesting that the patch can effectively prevent LV remodeling (Fig. 5A and B). In fact, in the I/R + P group, the patch implant limited the LV wall thinning compared with the I/R group (Fig. 5A).

Fluorescent images showed that cardiac Troponin and Connexin-43 protein content was markedly reduced 4 weeks after MI, whereas it was significantly preserved in the I/R + P group (0.64 ± 0.23 and 0.25 ± 0.09 RFI vs 1.16 ± 0.18 and 1.40 ± 0.19 RFI, respectively), reaching values more similar to the Sham group (1.38 ± 0.13 and 2.15 ± 0.35 RFI, respectively) (Fig. 5C and D). Connexin-43 lateralization was observed in the I/R group, as expected, being this altered gap junction distribution a typical feature of survived cardiomyocytes around the infarcted tissue (border zone). In the I/R + P group, instead, correct Connexin-43 distribution at the level of intercalated discs was evidenced (Fig. 5C). Although Connexin-43 appeared to be significantly reduced in the Sham + P compared to the Sham group, an in-depth analysis showed that this was true only after normalization against DAPI (Fig. S23A), while the unnormalized Cx43 was comparable in the two groups (Fig. S23B). This result suggests that an increased number of cells recruited in and under the patch (Fig. S23C and see below) might result in an apparent Cx43 reduction in the Sham + P group.

mRNA expression of important biomarkers was then evaluated through Real-Time PCR. Natriuretic peptides are autacoids with auto/paracrine effects that appear to protect cardiomyocytes from ischemia-reperfusion injury [73,74]. The expression and release of these natriuretic peptides by the myocardium can be sustained for many months or years after MI [75], and their levels have been shown to correlate with the magnitude of LV remodeling and dysfunction [73]. Specifically, a great deal of interest has focused on the relationship between cardiac performance following MI and the local release of natriuretic peptide B (BNP) [76], which has been investigated as a biomarker of acute coronary syndromes [77] and as a potential therapeutic agent [78]. BNP plays a role during the physiological growth of the heart and can stimulate proliferation and differentiation of fetal cardiomyocytes into mature ones [74,79]. The trend of BNP gene expression we observed in I/R + P animals was in line with previous studies [79] where it was hypothesized that the trend during phenotype differentiation was caused by differences in sequence genes, rate of transcription, and differential stabilization of the mRNA [80] (Fig. S24A).

Osteopontin, an extracellular matrix glycoprotein functioning as a cytokine, has been discussed in mediating vascular and myocardial damage in cardiovascular diseases [81] and in our study, as expected, it resulted significantly higher in animals with infarct compared to Sham and significantly decreased after MENDEP insertion (Fig. S24B).

3.3.4. Neovessel formation

Fluorescent image analysis of α-SMA revealed that in I/R + P hearts the region below MENDEP had a higher vessel density compared to the controls (Fig. 5E). Interestingly, quantification analysis of tubular structures and relative size in the tissue below the patch confirmed a significant increase in small vessels (<20 μm) in the I/R + P group compared to all the other groups. This increment was confirmed by vWF fluorescent intensity quantification (Fig. 5F–S25A and B).

α-SMA + circularly oriented cells were also observed inside the patches (Fig. 5G). In addition, at high magnification, the histological analysis highlighted the presence of cells, likely red blood cells, in the lumen of some neovessels, thus proving the active formation of functional blood vessels connected to host coronary circulation (Fig. 5H). The quantification of these neovessels inside the patch showed no significant difference between I/R + P and Sham + P groups (Fig. S25C) suggesting that MENDEP could promote neovessel formation irrespective of the presence of an infarct.

Together, these results indicated that epicardially implanted MENDEPs exhibited robust integration and enhanced blood vessel neoformation in the myocardium after I/R.

3.3.5. In vivo cell recruitment

It was demonstrated *in vitro* that MENDEP was able to attract cells. Consistently, cell recruitment was also observed in the *in vivo* model. In the hearts with the implanted patch, it was possible to observe several cells (both inside and under the patch) that stained positive for c-Kit and GATA-4 markers (Fig. 6A and C).

Based on literature findings, c-Kit + cells emerge as a stem cell population, either residing locally within specific cardiac niches or migrating from the circulatory system, exhibiting the capability to mainly differentiate into endothelial cells [82–89]. In our animal model, c-Kit + cells significantly increased in both Sham + P and I/R + P groups (Fig. 6A and B). While we cannot univocally infer the origin of these c-Kit + cells, however, the increased number of capillaries observed in the I/R + P group would suggest that some of them were resident and circulating precursors which are both responsible for neovessel formation.

GATA-4, a cardiogenic transcription factor essential during heart development, plays critical roles in cardiomyocyte proliferation, differentiation, survival, and hypertrophy [90–99]. In the adult heart, it is expressed by cardiomyocytes, albeit at low levels, and by NMCs, including some cardiac fibroblasts, where it contributes to enhancing angiogenesis [100]. In our study MENDEP induced a similar increase in GATA-4+ cells in both I/R + P and Sham + P groups, indicating that the recruitment of these cells was due to the properties of the patch (including controlled release of apelin) rather than to the infarction (Fig. 6C and D).

Lastly, it was possible to observe the recruitment of a few spindle-shaped cells both in the patch (Fig. 6E) and in the damaged area under the patch (Fig. 6F), where these cells became TnC-positive (Fig. 6F). Though interesting, however, this was an anecdotal observation and did not represent any demonstration that complete differentiation toward the cardiomyocyte lineage would follow.

3.3.6. In vivo degradation study

The *in vivo* degradation of the patch post-explant was assessed through morphological analysis (stereo optical microscopy and SEM) and FT-IR Chemical Imaging. Morphological characterization of the explanted patches was compared to pre-implantation samples, while FT-IR Chemical Imaging provided insights into the chemical composition of the patches retrieved from both Sham and I/R tissues, allowing for a detailed evaluation of their integration within the surrounding environment.

3.3.6.1. Morphological analysis before and after explant. SEM analysis was performed to compare the patch's surface and cross-section before implantation and after explantation from cardiac tissue. Fig. 7A–F illustrate the morphology of the explanted patches retrieved from I/R tissue, revealing their structural integration with ECM components, as corroborated by the histological analysis (Fig. S17). The epicardium-contacting surface of MENDEP appeared covered with globular ECM structures and cellular elements (Fig. 7D).

High-magnification SEM images (Fig. 7F) highlighted porosities (ranging from 2 to 7 μm in width, and from 10 to 20 μm in length, despite the treatment of the sample subjected to SEM analysis which may have collapsed the pores), which are conducive to cell colonization and vascularization (Fig. 5H and 6C).

The thickness of MENDEP was measured pre-implantation (216–220 μm) and post-explantation (ranging from 138 to 346 μm), suggesting non-uniform degradation due to the integration with the tissue. Additionally, gravimetric analysis on the retrieved patch indicated a 40–46 % mass loss under both I/R and Sham conditions compared to the original

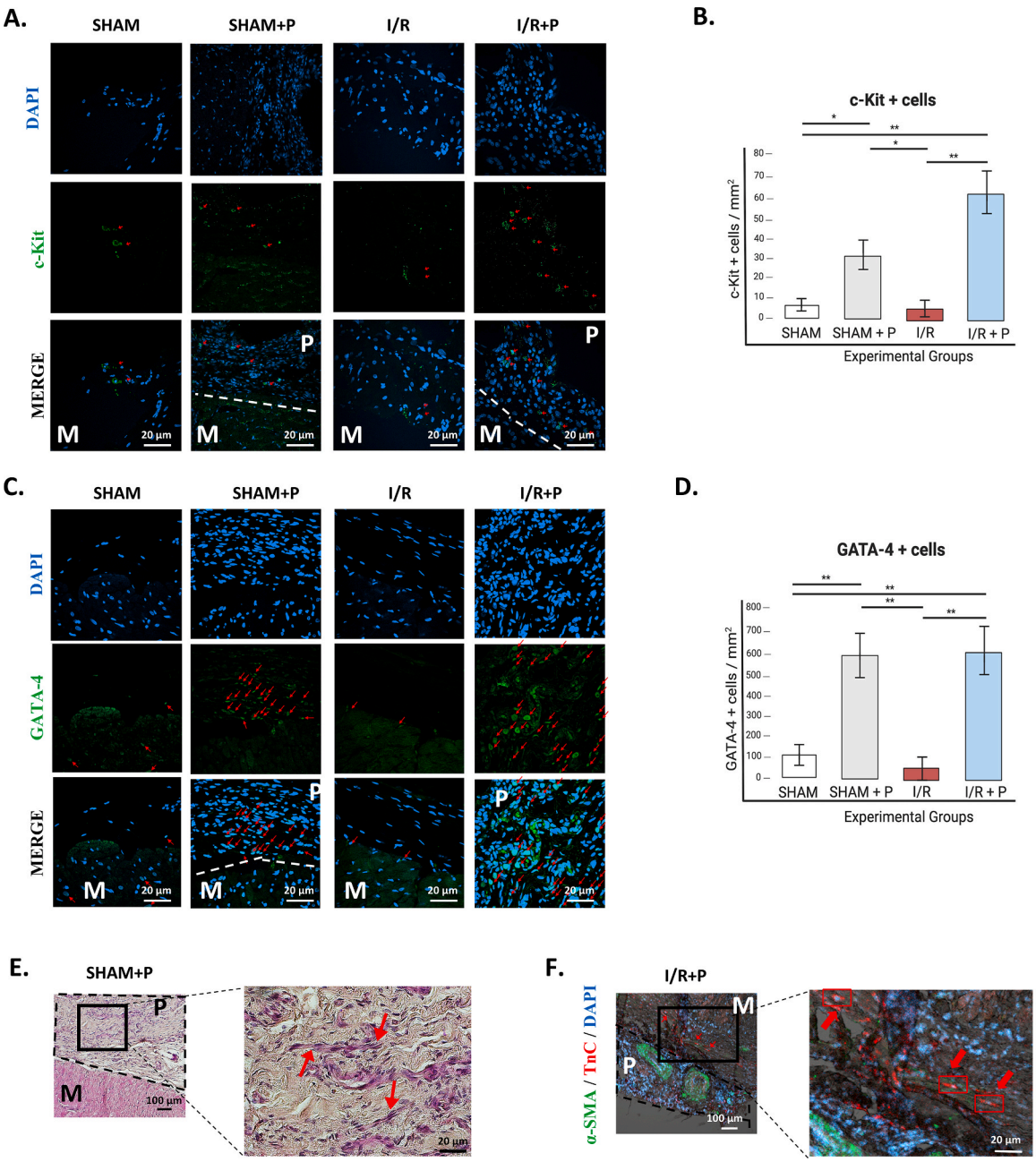

Fig. 6. MENDEP promotes stem cell recruitment. **A.** Representative confocal images showing c-Kit positive cell recruitment in both left ventricle of rat hearts and patch. Red arrows indicate c-Kit positive cells. **B.** Quantification of total c-Kit positive cells in three left ventricle regions for each experimental group, expressed as the number of cells per mm^2. c-Kit: green; DAPI: blue (n = 3). **C.** Representative confocal images showing GATA-4 positive cells recruited in both left ventricle of rat hearts and patch. Red arrows indicate GATA-4 positive cells. **D.** Quantification of total GATA-4 positive cells in three left ventricle regions for each experimental group, expressed as number of cells per mm^2. GATA-4: green; DAPI: blue (n = 3). **E.** Overview of the myocardium with implanted patch stained with H&E. Red arrows point to spindle-shaped into the patch at higher magnification (right). M: myocardium; P: patch. **F.** Representative confocal image of initial recruitment of TnC-positive spindle-shaped cells (red arrows) in rat hearts after MENDEP implantation. *p < 0.05, **p < 0.01, ***p < 0.001, by two-way ANOVA with Tukey's HSD post-hoc tests.

weight, confirming partial *in vivo* degradation. Stereomicroscope images (Figs. S26A and S26B) further illustrate the morphological changes of the patch.

3.3.6.2. -IR chemical imaging of the patch after explant. FT-IR Chemical Imaging was employed to analyze the chemical composition of the explanted patches and to better discriminate between the polymeric component of MENDEP and the biological matrix incorporating it. The analysis was performed on both sides of the explanted patch from Sham + P (Fig. 7G and H, S26C, S26E) and I/R + P (Fig. 7I and J, S26D, S26F) groups.

In Fig. 7G and I, on the left, the chemical maps of side A of the patch (epicardium-contacting surface) are reported, for the Sham + P and I/R + P groups respectively. These maps are plotted using as reference the characteristic peak of PLGA at 1750 cm^{-1} [16] showing that PLGA distribution in the sample is heterogeneous, indicating partial degradation. The presence of ECM components is confirmed by characteristic absorption bands, particularly at 1080 cm^{-1} (phosphodiester groups of nucleic acids [16,101]), at 1040 cm^{-1} (glycosaminoglycans, GAGs [16]), and a small band at 1730 cm^{-1} (cellular components, membrane

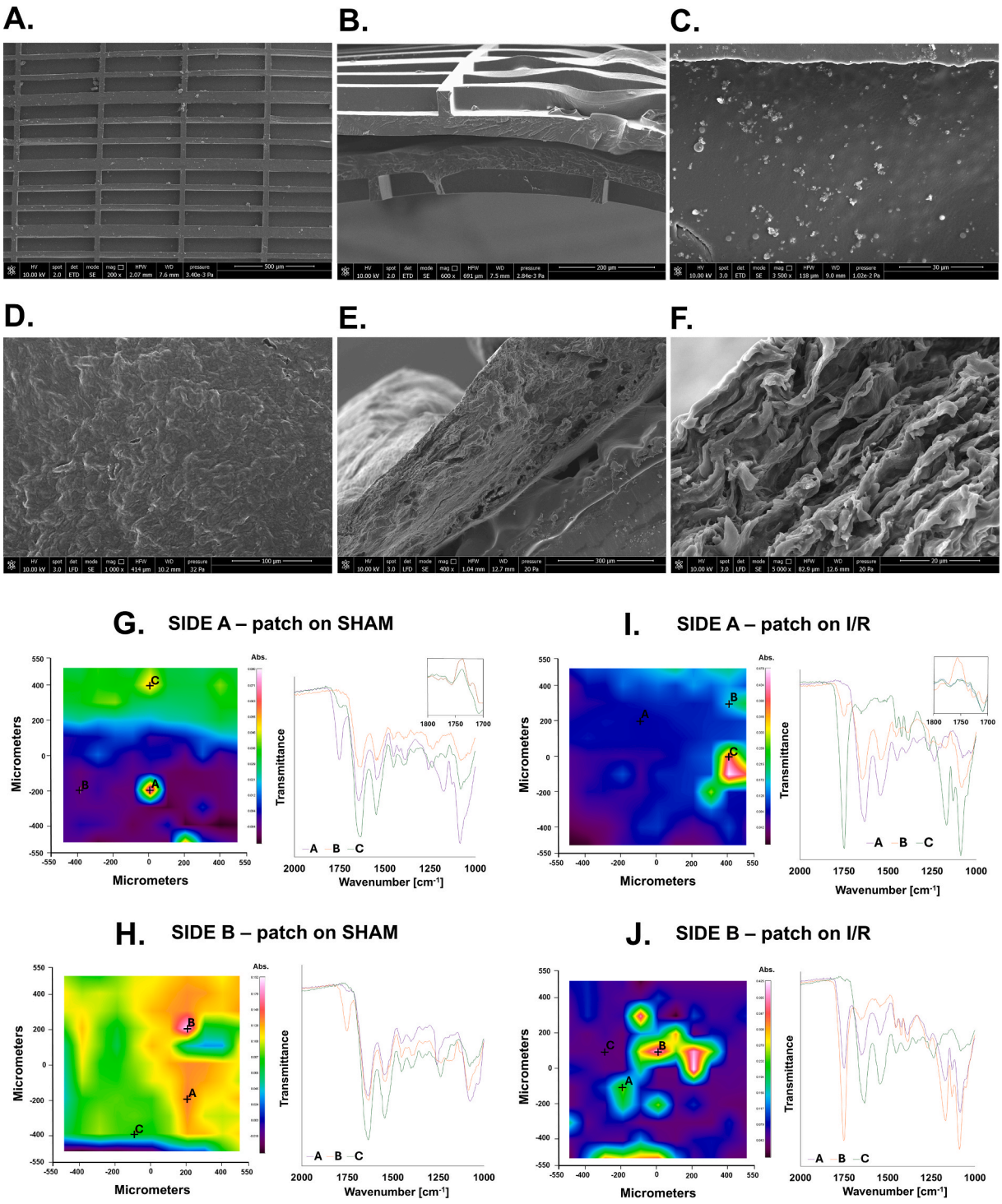

Fig. 7. SEM and FT-IR Chemical Imaging analysis of MENDEP (n = 3). A. SEM image of the microstructured and nano-functionalized surface of MENDEP (before implant). **B.** SEM image of the cross-section of MENDEP (before implant). **C.** SEM image showing a higher magnification of A., highlighting the nanoparticles inside one of the microstructure's cavities. **D.** SEM image of the epicardium-contacting surface of MENDEP retrieved from I/R explant. **E.** SEM image of the cross-section of MENDEP retrieved from I/R explant, showing the *continuum* of the patch merged with ECM. **F.** SEM image showing a higher magnification of E., highlighting the longitudinal form of the pores in the *continuum* of the patch merged with ECM, with dimensions suitable for vascularization. **G.** Chemical map (left) plotted using as reference the characteristic peak of PLGA at 1750 cm^{-1} and FT-IR spectra (right) corresponding to three selected points of the map (A, B, C) of "Side A" (epicardium-contacting surface) of MENDEP after Sham explant**.** Top, right: second derivative of the spectra highlighting the band at 1730 cm^{-1}. **H.** Chemical map (left) plotted using as reference the characteristic peak of PLGA at 1750 cm^{-1} and FT-IR spectra (right) corresponding to three selected points of the map (A, B, C) of "Side B" (epicardium-non-contacting surface) of MENDEP after Sham explant. Top, right: second derivative of the spectra highlighting the band at 1730 cm^{-1}. **I.** Chemical map (left) plotted using as reference the characteristic peak of PLGA at 1750 cm^{-1} and FT-IR spectra (right) corresponding to three selected points of the map (A, B, C) of "Side A" (epicardium-contacting surface) of MENDEP after I/R explant. **J.** Chemical map (left) plotted using as reference the characteristic peak of PLGA at 1750 cm^{-1} and FT-IR spectra (right) corresponding to three selected points of the map (A, B, C) of "Side B" (epicardium-non-contacting surface) of MENDEP after I/R explant.

phospholipids [16]) visible mostly in second derivative (Fig. 7G and I, top right). This landscape is further confirmed by the 3D visualization of the maps in Fig. S26; considering for example surface A (epicardium-contacting, Sham + P), it is possible to appreciate a residual profile of the microstructure of the polymeric patch (1750 cm^{-1} band, Fig. S26C, left), with an overlying layer of cellular components (1730 cm^{-1}, 1080 cm^{-1}, 1040 cm^{-1} bands Fig. S26E, left). Notably, structural preservation of the micropatterning is particularly significant as it suggests that MENDEP retains its bioactive topographical features, which are useful for continuing to direct cell signals for new tissue formation. Furthermore, chemical mapping of side B (external surface, epicardium non-contacting, Fig. 7H, left), indicates a higher PLGA content compared to side A, suggesting that degradation occurs more actively at the cardiac tissue interface. Spectral analysis (bottom right) reveals: similar ECM-related bands as side A, but with higher intensity at 1040 cm^{-1} (GAGs) and reduced absorption at 1730 cm^{-1}, indicating less cellular infiltration on side B. This suggests that tissue remodeling and polymer breakdown are more prominent on the epicardium-facing side (side A), where direct interaction with host cells and ECM deposition occurred.

Compared to the Sham + P samples, a greater reduction in PLGA content in I/R + P ones was observed (Fig. 7I and J), suggesting that MENDEP degrades more readily in infarcted tissue, likely due to the altered biochemical environment and increased enzymatic activity in the remodeling myocardium.

3.3.7. *FT-IR chemical imaging of the tissue under the patch after explant*

FT-IR Chemical Imaging was also used to evaluate the eventual differences in the biochemical signals of different sections of myocardial tissue (Figure S27 A-F). To give a quantitative evaluation, two parameters were examined: **a.** band ratio between glycosaminoglycan (GAG) and amide I (indicative of a cellularization process); **b.** band ratio between amide I and amide II (indicative of a protein asset). The obtained data showed how the highest value of the GAG/amide I ratio resulted in the one registered for I/R + P (0.10–0.30) against Sham (0.06–0.15) and I/R (0.15–0.20), indicating a proliferative and regenerative activity at the tissue level under the patch. On the contrary, the value of amide I/amide II ratio is higher for I/R tissue (1.7–2.1), indicating an alteration of the protein structure of the infarcted tissue, while in the sample I/R + P, the value of amide I/amide II ratio (1.6–1.8) is identical to that observed for Sham, that is indicative of the restoration of a more correct protein structure.

To evaluate the distribution of biodegradation products of the patch, (Figure S27 G-K), the maps were correlated with the characteristic peak of PLGA at 1750 cm^{-1} at two different areas of the cardiac tissue (proximal and distal to the patch). In the proximal point, peaks attributable to PLGA were observed, whereas in the distal point, no traces of the patch or its by-products were detected. This suggests the absorption of the by-products of the polymeric component relative to the biodegraded parts of MENDEP.

A more in-depth analysis was performed to evaluate the asset of the protein structure of myocardial tissue after explant. FT-IR Chemical Imaging enabled the second derivative analysis of protein spectra. PCA analysis obtained from chemical maps in μ-ATR for Sham, I/R and I/R + P groups were reported in Fig. 8A, B and C, respectively. From PCA analysis, showing a similar spectral variability characterized by a

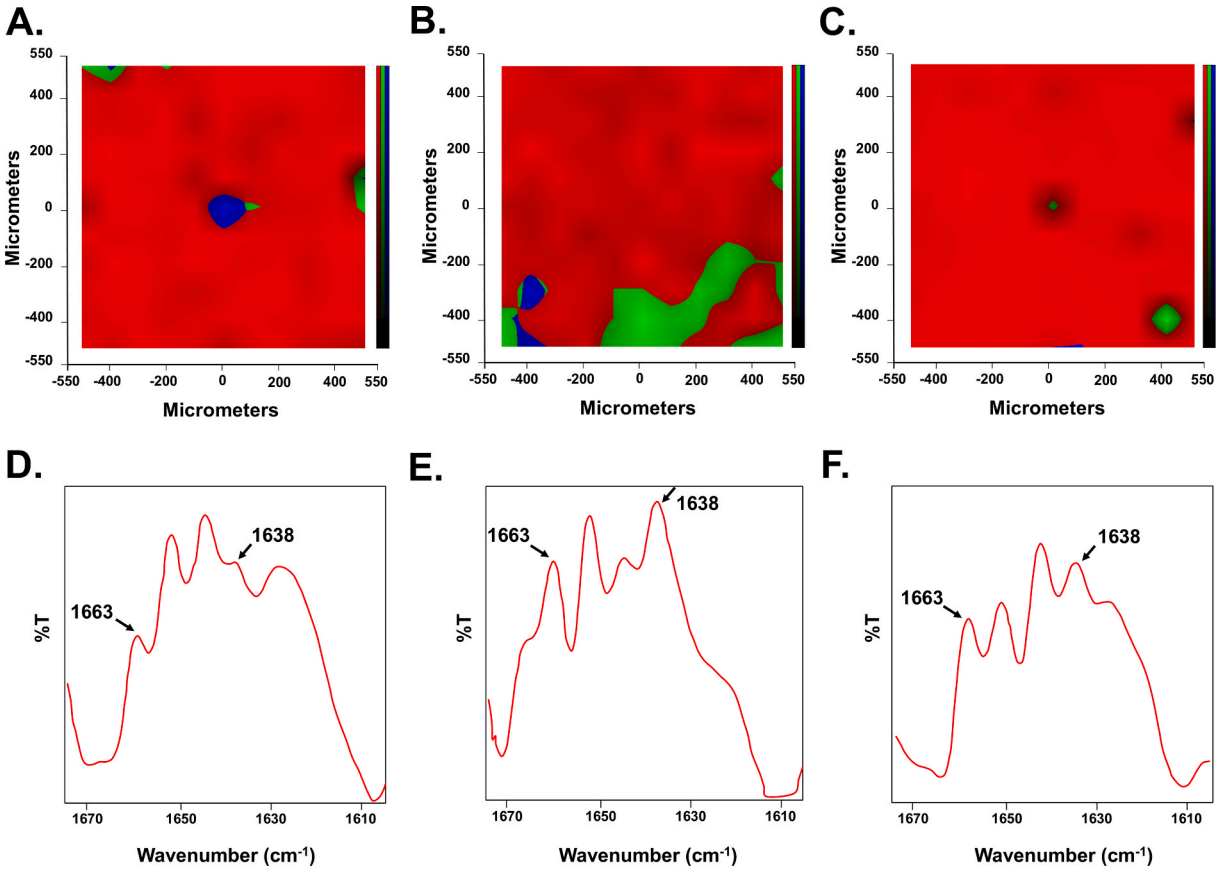

Fig. 8. FT-IR Chemical Imaging to evaluate protein conformational profile of myocardial tissue after MENDEP explant (n = 3). A. PCA analysis of deconvolution of amide I band for Sham myocardial tissue. **B.** PCA analysis of deconvolution of amide I band for myocardial tissue of I/R + P group. **C.** PCA analysis of deconvolution of amide I band for myocardial tissue of I/R + P group. **D.** Corresponding spectrum of amide I region acquired in A. **E.** Corresponding spectrum of amide I region acquired in B. **F.** Corresponding spectrum of amide I region acquired in C. Arrows indicate the bands at 1663 cm^{-1} (IR signal of collagen deposition) and 1638 cm^{-1} (IR signal of collagen triple helix deposition) showed in D, E and F.

predominant red area in all three samples, the second derivative spectra of the protein band were achieved (Fig. 8D, E and F). A conformational profile for the myocardial sample under the patch (Fig. 8F) was obtained resulting in a much more similar profile to that observed for the Sham (Fig. 8D) compared to the profile derived from the I/R chemical band (Fig. 8E). For example, the intensity of the band at 1663 cm^{-1} obtained by the deconvolution of amide I and indicative of collagen deposition for I/R + P (Fig. 8F) is comparable to that of the same band for Sham while it is much more intense in I/R tissue (Fig. 8E).

The same trend was observed for the band at 1638 cm^{-1} attributed to the triple helix of collagen which in I/R tissue is very evident, on the contrary, the intensity of this band in I/R treated with the patch is reduced moving towards the intensity of the Sham band.

Overall, the results suggest that the patch has both regenerative and protective effects in the area where the infarct occurred.

4. Discussion

To overcome the limitations of current MI therapies, in this study we developed MENDEP, an innovative bioartificial acellular cardiac patch endowed with (i) an electroconductive material, aiming at modulating cellular response and tissue regeneration; (ii) *in situ* release capability for delivering Apelin-13, a pleiotropic molecule exerting multiple biological effects including cardioprotection, fibrosis counteraction, chemoattraction, anti-inflammatory activity and angiogenesis promotion; (iii) MIP for correction of MMPs and their tissue inhibitors TIMPs unbalance involved in cardiac fibrosis.

MENDEP is a biomimetic scaffold specifically designed to replicate both the composition and structural organization of cardiac tissue, spanning from the micro-to the nanoscale. Its biomimetic properties are evident in several key aspects. The scaffold features a microstructured surface engineered to resemble the ECM of myocardial tissue, providing an environment conducive to cell adhesion and function [15]. At the nanoscale, the self-assembly of Fmoc-FF leads to the formation of nanofibers with diameters ranging from 20 to 100 nm, closely approximating the scale of collagen fibers, which are fundamental structural components of the ECM. These nanofibers not only mimic the morphology of natural ECM proteins and proteoglycans but also exhibit secondary structures such as β-sheets and α-helices, which play a crucial role in supporting cellular attachment and signaling. Supramolecular nanofibers with similar architectures have been demonstrated to be biocompatible [102,103] and capable of influencing cellular behavior through mechanotransduction and biochemical signaling pathways [104].

Another key biomimetic feature of MENDEP is its controlled biodegradability, reflecting the dynamic and transient nature of the native ECM. This property ensures gradual integration with the host tissue, allowing for progressive remodeling without generating undesirable inflammatory responses. Furthermore, MENDEP incorporates bioactive functionalization through the sustained release of Apelin-13, an endogenous cardiovascular regulatory molecule, which is stabilized by polymeric nanoparticles of natural origin. This targeted bioactivity enhances cell-matrix interactions and supports the physiological function of the repairing tissue. Additionally, MENDEP integrates molecularly imprinted nanoparticles designed to recognize and regulate MMP-9, a matrix metalloproteinase involved in ECM remodeling in cardiac tissue. By mimicking natural molecular recognition mechanisms such as antigen-antibody or ligand-receptor interactions, these nanoparticles help modulate MMP-9 activity, thereby preventing excessive ventricular remodeling and fibrosis.

In previous studies we have investigated a microfabricated PLGA/Gelatin bilayer scaffold incorporating an intermediate hydrogel layer for controlled drug release. Results demonstrated that, compared to the pure PLGA/Gelatin membrane (m-MP), the bilayer patch (MP) retained favorable mechanical properties - including elastic modulus and anisotropy - and exhibited similar biodegradation behavior under physiological conditions [15]. The possibility of providing a double microstructured interface for a better integration with the tissue, and an extensive surface nano-functionalization, stood for an interesting advancement. Furthermore, the bilayer consents the incorporation of an intermediate hydrogel layer to provide a versatile platform for sustained and controlled drug release, as demonstrated in adenosine delivery studies. In particular, we demonstrated that a multi-layered microstructured PLGA/Gelatin patch functionalized with adenosine (ADMMP) was able to favor *in vitro* stem cell adhesion, proliferation and early cardioinductivity [15]. Though endowed with full potential only for the treatment of acute disease, ADMMP showed an optimal adhesion on epicardial surface, cardioprotective effect and a non-fibrotic outcome at 3 months as results of an *in vivo* feasibility study using minipigs [16]. Leveraging on those previous achievements, we developed further to obtain MENDEP. In the present work, we deeply analyzed the properties of this acellular, clinically feasible, off-the-shelf potential therapeutic for cardiac repair.

A wide series of characterizations were performed on MENDEP, including physico-chemical (FT-IR Chemical Imaging, DSC, TGA), mechanical (DMA, Instron), degradation (GPC) and functional analyses (HPLC). Moreover, a conductivity analysis was carried out to verify the contribution of the Fmoc-FF peptide to the assembled system conductivity, using an impedance spectrometer. Considering the importance of good mechanical compliance of the patch with the myocardial tissue, an extensive study was performed by evaluating the viscoelastic properties of the patch at varying degradation time and frequency while providing mechanical support and preserving the mechanical anisotropy. Moreover, the patch resistance test to the suture and the burst resistance test, to simulate the biaxial forces to which the patch is subjected *in vivo* and to determine its resistance to prevent rupture or bleeding during the heartbeat, were performed using specific ISO standards for cardiovascular implants. Overall, MENDEP showed good mechanical properties and controlled biodegradability. In addition, Fmoc-FF incorporation increased the conductivity of the patch, thus reducing the electrical impedance of polymeric components. As expected, pure PLGA membranes exhibited high impedance, with Gelatin incorporation leading to an increase of the conductivity values. The addition of Fmoc-FF resulted in a further increase in conductivity. Moreover, the results showed improved conductivity when the Fmoc-FF hydrogel was used in the formulation of the patch, as shown by the comparison of MNDEP *vs* MENDEP. We have recently demonstrated [24] that Fmoc-FF alone or chemically conjugated with saccharides (e.g., glucosamine-6-sulphate) improves the conductivity of hydrogel patches targeting cardiac repair. This is an advantage to allow the intercellular electrical signal propagation, which combines maintaining biocompatibility and complete biodegradability of the patch. The combination of these properties can be considered an important advancement in developing patches for myocardial regeneration to facilitate clinical translation. Recently, epicardium patches were produced using non-degradable electroactive polymers by elevating electrically coupled contractility in infarcted myocardium. This approach allows *in situ* monitoring of mechano-physiological function and improvement of myocardial fibrosis. However, our study was oriented to obtain mainly a completely biodegradable and biocompatible patch for a passive electroconductivity approach, without the need for conductive activity as required in bioelectronic diagnosis [20]. Based on the above characterizations, MENDEP was demonstrated to possess high potentiality to be implanted on the infarcted wall where it acts as reinforcement, preventing wall stress and scarred area bulging. Indeed, several authors reported that mechanical support *per se* can reduce collagen synthesis and alignment, thus limiting the consequent adverse remodeling of the heart [105]. In addition, MENDEP also showed molecular recognition ability and controlled drug release activity that would further augment its therapeutic potentiality. *In vitro* evaluations confirmed that MIPs exhibited significantly higher affinity for MMP-9 compared to MMP-2 and TIMP-1. This selectivity suggests that, upon *in vivo* implantation,

the MIPs could effectively sequester excess MMP-9 without altering TIMP-1 or MMP-2 physiological levels, thereby mitigating pathological ECM remodeling while preserving essential proteolytic activity.

A key challenge in this system is the ability to prolong the activity of Apelin-13. Studies show that (Pyr)[1]Apelin-13, the predominant circulating isoform in cardiac tissue, exhibits an extremely short half-life [42]. To enhance the stability and prolong its release, we developed a formulation with PHB nanoparticles loaded onto the patch, demonstrating that MENDEP can prolong Apelin-13 release *in vitro*, ensuring a sustained and stable dose up to five days.

To prepare for the *in vivo* study, *in vitro* cytocompatibility, absence of sensitizing potential and cardioinductivity of patches were demonstrated.

The reported cardiomyogenic effect of our patch on NMCs, MSCs and hiPSCs is in our opinion a demonstration of the cardiac biomimetic environment offered by the patch *per se*, i.e., a 3D ambient, which resembles the native tissue histoarchitecture and is, therefore, able to dialogue on a molecular level with cardiac relevant cells. Indeed, a starting differentiation step could be obtained in both MSCs and NMCs, certainly not sufficient to direct their full cardiomyocyte specification. Regarding MSCs, the most prominent effect produced by our patch was GATA-4 upregulation, which we believe to not lead to their transdifferentiation into cardiomyocytes, but rather to a fine-tuning of MSC secretory activity toward a protective and pro-angiogenetic secretome. Indeed, there is recent compelling evidence that overexpression of GATA-4 in MSCs can promote cardioprotection and vascular angiogenesis effects through paracrine action [106,107]. A similar fine-tuning effect might be exerted on the NMC secretome as well, a possibility that deserves further investigation.

Further, *in vitro* migration tests showed that the chemoattractive capacity of MENDEP is due to Apelin-13 release, and conductive assays evidenced unaltered cell-cell interactions and cell beating synchronicity irrespective of patch functionalization.

MENDEP was then epicardially implanted in an experimental rat model of I/R. Overall, several positive effects could be experimentally evidenced. Our analyses revealed minimal fibrotic responses and robust tissue integration of MENDEP, highlighting its biocompatibility and ability to limit adverse foreign body reactions. By minimizing fibrotic encapsulation and promoting an anti-inflammatory microenvironment, MENDEP demonstrated its potential as a promising therapeutic platform for cardiac applications. MENDEP exerted neither adverse effects on the normal host myocardium (Sham + P group) nor vulnerability to arrhythmias. Further, MENDEP exhibited high levels of *in vivo* epicardial engraftment and improved the cellularized environment in the infarct area by, at least in part, promoting neovascularization and increasing cell retention. In particular, we hypothesize that prolonged and controlled patch-mediated Apelin-13 release allowed for the continued attraction of endogenous precursor cells, both c-Kit+ and GATA-4+, that could be observed at 4-week post-MI. Notably, NMCs comprise c-Kit+ and GATA-4+ cells as evidenced in the present and previous studies [52] and MSCs are c-Kit positive cells that acquire GATA-4 expression in response to culture on MENDEP. The recruitment of c-Kit+ and GATA-4+ cells, in both I/R + P and Sham + P groups, is thus consistent with the *in vitro* results showing MENDEP's ability to stimulate the migration of both NMCs and circulating MSCs. Therefore, we believe that some of the c-Kit+ and GATA-4+ cells recruited *in vivo* are indeed NMCs and MSCs.

Though the microstructured patches, mimicking the native tissue histoarchitecture, provided favorable niche conditions for the attracted endogenous cells, none of them exhibited mature 3D sarcomeric organization. However, neovascularization effects of MENDEP at the infarct region were evidenced, suggesting the attraction of resident and circulating precursors and their full differentiation as a major contributing factor, possibly in synergy with apelin-induced sprouting enhancement from existing vessels [41,108]. Interestingly, c-Kit + NMCs show the potential to give rise to new vessel formation [87,109,110]. In addition, NMCs and MSCs are widely recognized as capable of exerting important pro-regenerative and protective paracrine activities [82,111–115] on the surrounding injured myocardium.

Indeed, it is well known that an increase in vascularization can induce an improvement in cardiac function and vice versa [100, 116–119].

The findings of our *in vivo* study provide strong evidence of MENDEP's biodegradability and integration with cardiac tissue over the 4-week implantation period. The FT-IR Chemical Imaging maps and spectral data confirmed advanced polymer degradation at the tissue interface, active ECM deposition and cellular recruitment. Moreover, under the patch, the myocardial tissue appeared well preserved and cardiac gap junctions were found correctly distributed at the level of the intercalated discs. FT-IR Chemical Imaging allowed also to evaluate the tissue under the patch at a distal level of the myocardium, showing no traces of the patch or its by-products. This suggests the absorption of the by-products of the polymeric component relative to the biodegraded parts of MENDEP.

As for the efficacy of MIP-hMMP-9 functionalization to cardo LV remodeling, this was not easy to demonstrate. However, we observed that the mean fibrotic area detected in the I/R group (~21 %) was partially reduced in the I/R + P group (~14 %), suggesting that also this goal may have been, at least partially, achieved. The characteristics of this area were evaluated also in terms of protein asset using FT-IR Chemical Imaging. The results confirmed the capability of MENDEP of restoring a more correct asset of proteins suggesting the activation of the normal tissue reparative processes evolving in a non-fibrotic tissue. Altogether, both cardioprotective mechanisms and regenerative mechanisms appeared to be at the basis of the observed beneficial effects.

A few aspects that need more investigation could also be pointed out by the authors. Although *in vitro* results showed that MENDEP improved the cardiogenic maturation of both cardiac resident non-myocyte precursors and iPSC-CM, however, this effect could not be fully observed in the *in vivo* MI model. Only a few scattered TnC + cells showing an immature spindle-shaped appearance were observed in I/R + P cardiac slices, possibly representing an initial maturation step of cardiac precursors. Both immunofluorescent and histological assessments proved a wider surface of healthy cardiac tissue in I/R + P compared to I/R hearts and this was also supported by OPN increase; however, the assessment method adopted did not allow for discrimination between repair and prevention of cardiac damage. Also, whether the enhanced cellularization and neovascularization of MENDEP would significantly improve the cardiac function of the MI rat requires further investigation. We conducted a preliminary study of cMRI, demonstrating the firm fixation of MENDEP at rat heart and its passive extensibility following rhythmic contraction and relaxation motions. Interesting indications on the improvement of ejection fraction and stroke volume were observed in I/R + P rat compared to I/R rat, so further *in vivo* studies on evaluating the effects of MENDEP also on cardiac functions would be worthwhile.

The current work has multiple distinctive characteristics: (i) a greatly improved material design, good mechanical properties, high resistance to suture and burst, and reduced electrical impedance, while maintaining biodegradability; (ii) *functionalization 1* consisting of Apelin-13 release to provide cardioprotection and chemotactic recruitment of endogenous precursors (mesenchymal, endothelial, cardiac), necessary to maintain a complex cardiac tissue; (iii) *nano-functionalization 2* (MIP-hMMP-9) for contrasting ventricular remodeling through the restoration of the correct balance between MMP-9 and TIMP, thereby enhancing cardiac function; and (iv) *in vivo* 4-week development of MENDEP in a murine I/R-induced MI model to evaluate its potential therapeutic effect.

Although a detailed analysis of MENDEP degradation and interaction with host tissue after *in vivo* implantation was provided, a study of absorption over time *in vivo* would be interesting to be explored. However, to provide a reference point for long-term degradation, we highlight the MP patch (PLGA/Gelatin) study in minipigs, where complete

biodegradation and bioresorption were observed at 3 months post-implantation [16]. Given that the pig heart is a closer model to the human heart, this study serves as a valuable benchmark for MENDEP's expected degradation kinetics in future clinical applications.

In the future, a physiologically relevant large animal study, such as a porcine MI model, and a longer follow-up time will be employed as a more realistic experimental model to study the MENDEP integrated functional repair that was not fully observable in the current investigation. Moreover, developments in regulatory/safety aspects and scale-up of MENDEP production will significantly impact the ultimate clinical success of this innovative acellular cardiac engineering therapy. Further, mechanistic studies on myocardial repair pathways could also help extend the modes of action of this off-the-shelf cardiac therapy.

5. Conclusions

In conclusion, as a proof of concept, a microstructured, bioartificial, electroconductive and drug-eluting acellular patch, which is designed to attract endogenous precursor (stem) cells, favor their differentiation and contrast ventricular remodeling *in situ*, has been produced for the *in vivo* engineering of cardiac tissue. The developed MENDEP has a great potential to provide the desired therapeutic effect through endogenous cell recruitment and maturation, cardioprotection and ventricular remodeling counteraction, based on a previously unidentified implemented engineering design combining optimal biomimicry, controlled drug release, effective nano-functionalization, and simple manufacturing process. Although the mechanisms of action require further clarification, a paradigm has emerged for how adult epicardium may be activated for heart repair via our engineered, acellular, clinically feasible, *in vivo* cardiac patch application.

CRediT authorship contribution statement

Caterina Cristallini: Writing – review & editing, Writing – original draft, Validation, Supervision, Investigation, Funding acquisition, Data curation, Conceptualization. **Daniela Rossin:** Writing – review & editing, Writing – original draft, Visualization, Investigation, Formal analysis. **Roberto Vanni:** Writing – review & editing, Investigation, Formal analysis. **Niccoletta Barbani:** Investigation, Formal analysis. **Chiara Bulgheresi:** Visualization, Validation, Investigation, Formal analysis, Data curation. **Massimiliano Labardi:** Writing – review & editing, Investigation, Formal analysis, Data curation. **Sadia Perveen:** Investigation, Formal analysis. **Silvia Burchielli:** Writing – review & editing, Validation, Resources, Investigation, Data curation. **Domiziana Terlizzi:** Validation, Investigation. **Claudia Kusmic:** Writing – review & editing, Visualization, Validation, Investigation, Formal analysis, Data curation. **Silvia Del Ry:** Writing – review & editing, Investigation, Formal analysis, Data curation. **Manuela Cabiati:** Visualization, Investigation, Formal analysis, Data curation. **Cheherazade Trouki:** Writing – review & editing, Visualization, Investigation, Formal analysis, Data curation. **Dawid Rossino:** Writing – review & editing, Visualization, Formal analysis, Data curation. **Francesca Sergi:** Investigation, Formal analysis, Data curation. **Anthea Villano:** Investigation, Formal analysis, Data curation. **Giovanni D. Aquaro:** Investigation. **Giorgia Scarpellino:** Investigation, Formal analysis. **Federico A. Ruffinatti:** Writing – review & editing, Formal analysis. **Sara Amorim:** Investigation, Data curation. **Ricardo A. Pires:** Supervision, Investigation, Formal analysis. **Rui L. Reis:** Supervision, Funding acquisition. **Raffaella Rastaldo:** Writing – review & editing, Writing – original draft, Supervision, Funding acquisition, Conceptualization. **Claudia Giachino:** Writing – review & editing, Writing – original draft, Supervision, Funding acquisition, Conceptualization.

Ethics approval and consent to participate

The *in vivo* experimental activity on the rat animal model was performed at the Centro di Biomedicina Sperimentale (CBS), Research Area of the CNR (Pisa, Italy), after authorization no. 536/2020-PR on May 27, 2020 delivered by the Experimental Animal Ethics Committee of the Italian Ministry of Health.

Declaration of competing interests

Caterina Cristallini reports financial support was provided by EU project INCIPIT M-ERA.NET 2 call 2016, MIUR FIRST. Claudia Giachino reports financial support was provided by Compagnia di San Paolo Foundation. Raffaella Rastaldo reports financial support was provided by local funds Rilo RASR_RILO_23_01. Claudia Giachino reports financial support was provided by local funds GIAC_RILO_23_02. Caterina Cristallini, Claudia Giachino, Raffaella Rastaldo and Cheherazade Trouki report financial support was provided by European Union - NextGenerationEU, Mission 4, Component 2, Investment 1.1, financed within PRIN 2022 D.D. n. 104 02-02-2022 - 2022ATB4TP - Innovative development of a cardiac patch in the industrialization phase for the activation of regenerative and protective processes of cardiac ischemic issues, CUP D53D23013370006, B53D23020090006. Caterina Cristallini, Raffaella Rastaldo, Claudia Giachino, Niccoletta Barbani, Massimiliano Labardi, Sara Amorim, Ricardo A. Pires, Rui L. Reis has patent pending to University of Turin, CNR. Rui L. Reis is an associate editor for Bioactive Materials and was not involved in the editorial review or the decision to publish this article. If there are other authors, they declare that they have no known competing financial interests or personal relationships that could have appeared to influence the work reported in this paper.

Acknowledgements

This research study was supported by transnational EU project INCIPIT M-ERA.NET 2 call 2016, MIUR (DD n. 1218, June 21, 2019) FIRST; PoC Instrument-II cut-off 2020, Fondazione Compagnia di San Paolo (Compagnia di San Paolo Foundation); this work was partially supported by European Union - NextGenerationEU, Mission 4, Component 2, Investment 1.1, financed within PRIN 2022 D.D. n. 104 02-02-2022 - 2022ATB4TP - Innovative development of a cardiac patch in the industrialization phase for the activation of regenerative and protective processes of cardiac ischemic issues, CUP D53D23013370006, B53D23020090006. This work was also partially supported by local funds RASR_RILO_23_01 and GIAC_RILO_23_02.

The authors also acknowledge the contribution of Luca Munaron for assistance in electrophysiological experimental design; Rachele Rosso, Lelio Sciulli, Emanuela Vitale, Matteo Aubry, Marco Lo Iacono and Erika Fiorino for assistance in cellular and molecular analyses.

The graphical abstract was in part created with BioRender.com.

Appendix A. Supplementary data

Supplementary data to this article can be found online at https://doi.org/10.1016/j.bioactmat.2025.04.008.

References

[1] N. Salari, F. Morddarvanjoghi, A. Abdolmaleki, S. Rasoulpoor, A.A. Khaleghi, L. A. Hezarkhani, S. Shohaimi, M. Mohammadi, The global prevalence of myocardial infarction: a systematic review and meta-analysis, BMC Cardiovasc. Disord. 23 (2023) 206, https://doi.org/10.1186/s12872-023-03231-w.

[2] V. Deshmukh, J. Wang, J.F. Martin, Leading progress in heart regeneration and repair, Curr. Opin. Cell Biol. 61 (2019) 79–85, https://doi.org/10.1016/j.ceb.2019.07.005.

[3] P.L. Laforgia, C. Auguadro, S. Bronzato, A. Durante, The reduction of mortality in acute myocardial infarction: from bed rest to future directions, Int. J. Prev. Med. 13 (2022) 56, https://doi.org/10.4103/ijpvm.IJPVM_122_20.

[4] B. Hegyi, J. Bossuyt, L.G. Griffiths, R. Shimkunas, Z. Coulibaly, Z. Jian, K. N. Grimsrud, C.S. Sondergaard, K.S. Ginsburg, N. Chiamvimonvat, et al., Complex electrophysiological remodeling in postinfarction ischemic heart failure, Proc. Natl. Acad. Sci. 115 (2018), https://doi.org/10.1073/pnas.1718211115.

[5] E.K. Lamb, G.W. Kao, R.L. Kao, Cellular cardiomyoplasty: its past, present, and future, Methods Mol. Biol. 1036 (2013) 1–17, https://doi.org/10.1007/978-1-62703-511-8_1.

[6] T. Sadahiro, S. Yamanaka, M. Ieda, Direct cardiac reprogramming, Circ. Res. 116 (2015) 1378–1391, https://doi.org/10.1161/CIRCRESAHA.116.305374.

[7] K. Huang, E.W. Ozpinar, T. Su, J. Tang, D. Shen, L. Qiao, S. Hu, Z. Li, H. Liang, K. Mathews, et al., An off-the-shelf artificial cardiac patch improves cardiac repair after myocardial infarction in rats and pigs, Sci. Transl. Med. 12 (2020), https://doi.org/10.1126/scitranslmed.aat9683.

[8] S. McMahan, A. Taylor, K.M. Copeland, Z. Pan, J. Liao, Y. Hong, Current advances in biodegradable synthetic polymer based cardiac patches, J. Biomed. Mater. Res. 108 (2020) 972–983, https://doi.org/10.1002/jbm.a.36874.

[9] A. Shpigel, D.L. Brown, Mechanical Complications of Acute Myocardial Infarction, in: Cardiac Intensive Care, Elsevier, 2019, pp. 160–165.e2.

[10] S. Perveen, D. Rossin, E. Vitale, R. Rosso, R. Vanni, C. Cristallini, R. Rastaldo, C. Giachino, Therapeutic acellular scaffolds for limiting left ventricular remodelling-current status and future directions, Int. J. Mol. Sci. 22 (2021), https://doi.org/10.3390/ijms222313054.

[11] U. Sarig, H. Sarig, E. de-Berardinis, S.-Y. Chaw, E.B.V. Nguyen, V.S. Ramanujam, V.D. Thang, M. Al-Haddawi, S. Liao, D. Seliktar, et al., Natural myocardial ECM patch drives cardiac progenitor based restoration even after scarring, Acta Biomater. 44 (2016) 209–220, https://doi.org/10.1016/j.actbio.2016.08.031.

[12] G.I. Barbulescu, F.M. Bojin, V.L. Ordodi, I.D. Goje, A.S. Barbulescu, V. Paunescu, Decellularized extracellular matrix scaffolds for cardiovascular tissue engineering: current techniques and challenges, Int. J. Mol. Sci. 23 (2022), https://doi.org/10.3390/ijms232113040.

[13] A. D'Amore, T. Yoshizumi, S.K. Luketich, M.T. Wolf, X. Gu, M. Cammarata, R. Hoff, S.F. Badylak, W.R. Wagner, Bi-layered polyurethane – extracellular matrix cardiac patch improves ischemic ventricular wall remodeling in a rat model, Biomaterials 107 (2016) 1–14, https://doi.org/10.1016/j.biomaterials.2016.07.039.

[14] S. Pok, I.V. Stupin, C. Tsao, R.G. Pautler, Y. Gao, R.M. Nieto, Z. Tao, C.D. Fraser, A.V. Annapragada, J.G. Jacot, Full-thickness heart repair with an engineered multilayered myocardial patch in rat model, Adv Healthc Mater 6 (2017), https://doi.org/10.1002/adhm.201600549.

[15] C. Cristallini, E. Cibrario Rocchietti, M. Gagliardi, L. Mortati, S. Saviozzi, E. Bellotti, V. Turinetto, M.P. Sassi, N. Barbani, C. Giachino, Micro- and macrostructured PLGA/Gelatin scaffolds promote early cardiogenic commitment of human mesenchymal stem cells in vitro, Stem Cells Int 2016 (2016) 1–16, https://doi.org/10.1155/2016/7176154.

[16] C. Cristallini, G. Vaccari, N. Barbani, E. Cibrario Rocchietti, R. Barberis, M. Falzone, K. Cabiale, G. Perona, E. Bellotti, R. Rastaldo, et al., Cardioprotection of PLGA/gelatine cardiac patches functionalised with adenosine in a large animal model of ischaemia and reperfusion injury: a feasibility study, J Tissue Eng Regen Med 13 (2019) 1253–1264, https://doi.org/10.1002/term.2875.

[17] H. Esmaeili, A. Patino-Guerrero, M. Hasany, M.O. Ansari, A. Memic, A. Dolatshahi-Pirouz, M. Nikkhah, Electroconductive biomaterials for cardiac tissue engineering, Acta Biomater. 139 (2022) 118–140, https://doi.org/10.1016/j.actbio.2021.08.031.

[18] Y. Liang, A. Mitriashkin, T.T. Lim, J.C.-H. Goh, Conductive polypyrrole-encapsulated silk fibroin fibers for cardiac tissue engineering, Biomaterials 276 (2021) 121008, https://doi.org/10.1016/j.biomaterials.2021.121008.

[19] K. Roshanbinfar, M. Schiffer, E. Carls, M. Angeloni, M. Koleśnik-Gray, S. Schruefer, D.W. Schubert, F. Ferrazzi, V. Krstić, B.K. Fleischmann, et al., Electrically conductive collagen-PEDOT:PSS hydrogel prevents post-infarct cardiac arrhythmia and supports HiPSC-cardiomyocyte function, Adv. Mater. 36 (2024), https://doi.org/10.1002/adma.202403642.

[20] C. Yu, M. Shi, S. He, M. Yao, H. Sun, Z. Yue, Y. Qiu, B. Liu, L. Liang, Z. Zhao, et al., Chronological adhesive cardiac patch for synchronous mechanophysiological monitoring and electrocoupling therapy, Nat. Commun. 14 (2023) 6226, https://doi.org/10.1038/s41467-023-42008-9.

[21] K. Tao, A. Levin, L. Adler-Abramovich, E. Gazit, Fmoc-modified amino acids and short peptides: simple bio-inspired building blocks for the fabrication of functional materials, Chem. Soc. Rev. 45 (2016) 3935–3953, https://doi.org/10.1039/C5CS00889A.

[22] A. Brito, Y.M. Abul-Haija, D.S. da Costa, R. Novoa-Carballal, R.L. Reis, R.V. Ulijn, R.A. Pires, I. Pashkuleva, Minimalistic supramolecular proteoglycan mimics by Co-assembly of aromatic peptide and carbohydrate amphiphiles, Chem. Sci. 10 (2019) 2385–2390, https://doi.org/10.1039/C8SC04361B.

[23] V.I.B. Castro, A.R. Araújo, F. Duarte, A. Sousa-Franco, R.L. Reis, I. Pashkuleva, R. A. Pires, Glycopeptide-based supramolecular hydrogels induce differentiation of adipose stem cells into neural lineages, ACS Appl. Mater. Interfaces 15 (2023) 29998–30007, https://doi.org/10.1021/acsami.3c05309.

[24] V.I.B. Castro, S. Amorim, D. Caballero, C.M. Abreu, S.C. Kundu, R.L. Reis, I. Pashkuleva, R.A. Pires, Patterned glycopeptide-based supramolecular hydrogel promotes the alignment and contractility of IPSC-derived cardiomyocytes, Biomater. Adv. 167 (2025) 214091, https://doi.org/10.1016/j.bioadv.2024.214091.

[25] Z. Fan, L. Sun, Y. Huang, Y. Wang, M. Zhang, Bioinspired fluorescent dipeptide nanoparticles for targeted cancer cell imaging and real-time monitoring of drug release, Nat. Nanotechnol. 11 (2016) 388–394, https://doi.org/10.1038/nnano.2015.312.

[26] K. Tao, P. Makam, R. Aizen, E. Gazit, Self-assembling peptide semiconductors, Science 2017 (1979) 358, https://doi.org/10.1126/science.aam9756.

[27] M.A.S. Moore, K. Hattori, B. Heissig, J.-H. Shieh, S. Dias, R.G. Crystal, S. Rafii, Mobilization of endothelial and hematopoietic stem and progenitor cells by adenovector-mediated elevation of serum levels of SDF-1, VEGF, and angiopoietin-1, Ann. N. Y. Acad. Sci. 938 (2001) 36–47, https://doi.org/10.1111/j.1749-6632.2001.tb03572.x.

[28] T. Takahashi, C. Kalka, H. Masuda, D. Chen, M. Silver, M. Kearney, M. Magner, J. M. Isner, T. Asahara, Ischemia- and cytokine-induced mobilization of bone marrow-derived endothelial progenitor cells for neovascularization, Nat Med 5 (1999) 434–438, https://doi.org/10.1038/7434.

[29] M.S. Penn, Importance of the SDF-1:CXCR4 Axis in myocardial repair, Circ. Res. 104 (2009) 1133–1135, https://doi.org/10.1161/CIRCRESAHA.109.198929.

[30] D. Tempel, M. de Boer, E.D. van Deel, R.A. Haasdijk, D.J. Duncker, C. Cheng, S. Schulte-Merker, H.J. Duckers, Apelin enhances cardiac neovascularization after myocardial infarction by recruiting Aplnr+ circulating cells, Circ. Res. 111 (2012) 585–598, https://doi.org/10.1161/CIRCRESAHA.111.262097.

[31] D. Rossin, R. Vanni, M. Lo Iacono, C. Cristallini, C. Giachino, R. Rastaldo, APJ as promising therapeutic target of peptide analogues in myocardial infarction- and hypertension-induced heart failure, Pharmaceutics 15 (2023) 1408, https://doi.org/10.3390/pharmaceutics15051408.

[32] F.A. Chapman, J.J. Maguire, D.E. Newby, A.P. Davenport, N. Dhaun, Targeting the apelin system for the treatment of cardiovascular diseases, Cardiovasc. Res. 119 (2023) 2683–2696, https://doi.org/10.1093/cvr/cvad171.

[33] W. Liu, J. Yan, W. Pan, M. Tang, Apelin/elabela-APJ: a novel therapeutic target in the cardiovascular system, Ann. Transl. Med. 8 (2020) 243, https://doi.org/10.21037/atm.2020.02.07.

[34] T. Sato, A. Kadowaki, T. Suzuki, H. Ito, H. Watanabe, Y. Imai, K. Kuba, Loss of apelin augments angiotensin II-induced cardiac dysfunction and pathological remodeling, Int. J. Mol. Sci. 20 (2019) 239, https://doi.org/10.3390/ijms20020239.

[35] E. Vitale, R. Rosso, M. Lo Iacono, C. Cristallini, C. Giachino, R. Rastaldo, Apelin-13 increases functional connexin-43 through autophagy inhibition via AKT/MTOR pathway in the non-myocytic cell population of the heart, Int. J. Mol. Sci. 23 (2022) 13073, https://doi.org/10.3390/ijms232113073.

[36] A. Folino, L. Accomasso, C. Giachino, P.G. Montarolo, G. Losano, P. Pagliaro, R. Rastaldo, Apelin-induced cardioprotection against ischaemia/reperfusion injury: roles of epidermal growth factor and src, Acta Physiol. 222 (2018) e12924, https://doi.org/10.1111/apha.12924.

[37] C.A. Makarewich, A.Z. Munir, G.G. Schiattarella, S. Bezprozvannaya, O. N. Raguimova, E.E. Cho, A.H. Vidal, S.L. Robia, R. Bassel-Duby, E.N. Olson, The DWORF micropeptide enhances contractility and prevents heart failure in a mouse model of dilated cardiomyopathy, Elife 7 (2018), https://doi.org/10.7554/eLife.38319.

[38] W. Wang, S.M.K. McKinnie, V.B. Patel, G. Haddad, Z. Wang, P. Zhabyeyev, S. K. Das, R. Basu, B. McLean, V. Kandalam, et al., Loss of apelin exacerbates myocardial infarction adverse remodeling and ischemia-reperfusion injury: therapeutic potential of synthetic apelin analogues, J. Am. Heart Assoc. 2 (2013), https://doi.org/10.1161/JAHA.113.000249.

[39] N.K. Zhang, Y. Cao, Z.M. Zhu, N. Zheng, L. Wang, X.H. Xu, L.R. Gao, Activation of endogenous cardiac stem cells by apelin-13 in infarcted rat heart, Cell Transplant. 25 (2016) 1645–1652, https://doi.org/10.3727/096368916X691123.

[40] X. Wang, L. Zhang, P. Li, Y. Zheng, Y. Yang, S. Ji, Apelin/APJ system in inflammation, Int. Immunopharmacol. 109 (2022) 108822, https://doi.org/10.1016/j.intimp.2022.108822.

[41] C.S. Helker, J. Eberlein, K. Wilhelm, T. Sugino, J. Malchow, A. Schuermann, S. Baumeister, H.-B. Kwon, H.-M. Maischein, M. Potente, et al., Apelin signaling drives vascular endothelial cells toward a pro-angiogenic state, Elife 9 (2020), https://doi.org/10.7554/eLife.55589.

[42] J.M. Onorato, C. Xu, X.-Q. Chen, A.V. Rose, C. Generaux, K. Lentz, P. Shipkova, S. Arthur, J.K. Hennan, R. Haskell, et al., Linking (Pyr)1apelin-13 pharmacokinetics to efficacy: stabilization and measurement of a high clearance peptide in rodents, Anal. Biochem. 568 (2019) 41–50, https://doi.org/10.1016/j.ab.2018.12.022.

[43] V. Serpooshan, S. Sivanesan, X. Huang, M. Mahmoudi, A.V. Malkovskiy, M. Zhao, M. Inayathullah, D. Wagh, X.J. Zhang, S. Metzler, et al., [Pyr1]-Apelin-13 delivery via nano-liposomal encapsulation attenuates pressure overload-induced cardiac dysfunction, Biomaterials 37 (2015) 289–298, https://doi.org/10.1016/j.biomaterials.2014.08.045.

[44] T. Pulingam, J.N. Appaturi, T. Parumasivam, A. Ahmad, K. Sudesh, Biomedical applications of polyhydroxyalkanoate in tissue engineering, Polymers 14 (2022) 2141, https://doi.org/10.3390/polym14112141.

[45] C.S. Webb, D.D. Bonnema, S.H. Ahmed, A.H. Leonardi, C.D. McClure, L.L. Clark, R.E. Stroud, W.C. Corn, L. Finklea, M.R. Zile, et al., Specific temporal profile of matrix metalloproteinase release occurs in patients after myocardial infarction, Circulation 114 (2006) 1020–1027, https://doi.org/10.1161/CIRCULATIONAHA.105.600353.

[46] C. Cristallini, M. Gagliardi, N. Barbani, D. Giannessi, G.D. Guerra, Novel biodegradable, biomimetic and functionalised polymer scaffolds to prevent expansion of post-infarct left ventricular remodelling, Proceedings of the Journal of Materials Science: Materials in Medicine 23 (2012) 205–216.

[47] A. Villano, G. Barcaro, S. Monti, N. Barbani, A. Rizzo, D. Rossin, R. Rastaldo, C. Giachino, C. Cristallini, Molecularly imprinted nanoparticles towards MMP9 for controlling cardiac ECM after myocardial infarction: a predictive experimental-computational chemistry investigation, Biomedicines 10 (2022), https://doi.org/10.3390/biomedicines10092070.

[48] L. Wang, Y. Liu, G. Ye, Y. He, B. Li, Y. Guan, B. Gong, K. Mequanint, M.M.Q. Xing, X. Qiu, Injectable and conductive cardiac patches repair infarcted myocardium in rats and minipigs, Nat. Biomed. Eng. 5 (2021) 1157–1173, https://doi.org/10.1038/s41551-021-00796-9.

[49] F. He, S.M. Andrabi, H. Shi, Y. Son, H. Qiu, J. Xie, W. Zhu, Sequential delivery of cardioactive drugs via microcapped microneedle patches for improved heart function in post myocardial infarction rats, Acta Biomater. 192 (2025) 235–247, https://doi.org/10.1016/j.actbio.2024.12.009.
[50] X. Wang, H. Wang, X. Liu, Y. Zhang, J. Li, H. Liu, J. Feng, W. Jiang, L. Liu, Y. Chen, et al., Self-adhesion conductive cardiac patch based on methoxytriethylene glycol-functionalized graphene effectively improves cardiac function after myocardial infarction, J. Adv. Res. (2024), https://doi.org/10.1016/j.jare.2024.11.026.
[51] W. Rudzinski, W. Plazinski, Studies of the kinetics of solute adsorption at solid/solution interfaces: on the possibility of distinguishing between the diffusional and the surface reaction kinetic models by studying the pseudo-first-order kinetics, J. Phys. Chem. C 111 (2007) 15100–15110, https://doi.org/10.1021/jp073249c.
[52] C. Cristallini, E. Cibrario Rocchietti, L. Accomasso, A. Folino, C. Gallina, L. Muratori, P. Pagliaro, R. Rastaldo, S. Raimondo, S. Saviozzi, et al., The effect of bioartificial constructs that mimic myocardial structure and biomechanical properties on stem cell commitment towards cardiac lineage, Biomaterials 35 (2014) 92–104, https://doi.org/10.1016/j.biomaterials.2013.09.058.
[53] M. Cabiati, C. Salvadori, A. Sapio, S. Burchielli, L. Carlucci, S. Moscato, L. Sabatino, C. Caselli, L. Mattii, S. Del Ry, Aging and biomarkers: transcriptional levels evaluation of osteopontin/MiRNA-181a Axis in hepatic tissue of rats in different age ranges, Exp. Gerontol. 133 (2020) 110879, https://doi.org/10.1016/j.exger.2020.110879.
[54] S.A. Bustin, V. Benes, J.A. Garson, J. Hellemans, J. Huggett, M. Kubista, R. Mueller, T. Nolan, M.W. Pfaffl, G.L. Shipley, et al., The MIQE guidelines: minimum information for publication of quantitative real-time PCR experiments, Clin. Chem. 55 (2009) 611–622, https://doi.org/10.1373/clinchem.2008.112797.
[55] M. Alonzo, M. Delgado, C. Cleetus, S.A. Kumar, V. Thakur, M. Chattopadhyay, B. Joddar, Methods for histological characterization of cryo-induced myocardial infarction in a rat model, Acta Histochem. 122 (2020) 151624, https://doi.org/10.1016/j.acthis.2020.151624.
[56] W. Rudzinski, W. Plazinski, Kinetics of solute adsorption at solid/solution interfaces: a theoretical development of the empirical pseudo-first and pseudo-second order kinetic rate equations, based on applying the statistical rate theory of interfacial transport, J. Phys. Chem. B 110 (2006) 16514–16525, https://doi.org/10.1021/jp061779n.
[57] S. Ramadan, N. Paul, H.E. Naguib, Standardized static and dynamic evaluation of myocardial tissue properties, Biomedical Materials 12 (2017) 025013, https://doi.org/10.1088/1748-605X/aa57a5.
[58] H. Tsuji, T. Hayashi, Hydrolytic degradation and crystallization behavior of linear 2-armed and star-shaped 4-armed poly(L-lactide)s: effects of branching architecture and crystallinity, J. Appl. Polym. Sci. 132 (2015), https://doi.org/10.1002/app.41983.
[59] P. Gentile, V. Chiono, I. Carmagnola, P. Hatton, An overview of poly(lactic-Co-glycolic) acid (PLGA)-Based biomaterials for bone tissue engineering, Int. J. Mol. Sci. 15 (2014) 3640–3659, https://doi.org/10.3390/ijms15033640.
[60] M. Pensalfini, S. Meneghello, V. Lintas, K. Bircher, A.E. Ehret, E. Mazza, The suture retention test, revisited and revised, J. Mech. Behav. Biomed. Mater. 77 (2018) 711–717, https://doi.org/10.1016/j.jmbbm.2017.08.021.
[61] E.G. Roberts, E.L. Lee, D. Backman, J.A. Buczek-Thomas, S. Emani, J.Y. Wong, Engineering myocardial tissue patches with hierarchical structure–function, Ann. Biomed. Eng. 43 (2015) 762–773, https://doi.org/10.1007/s10439-014-1210-6.
[62] D. Freytes, A. Rundell, J. Vandegeest, D. Vorp, T. Webster, S. Badylak, Analytically derived material properties of multilaminated extracellular matrix devices using the ball-burst test, Biomaterials 26 (2005) 5518–5531, https://doi.org/10.1016/j.biomaterials.2005.01.070.
[63] C. Xu, C. Okpokwasili, Y. Huang, X. Shi, J. Wu, J. Liao, L. Tang, Y. Hong, Optimizing anisotropic polyurethane scaffolds to mechanically match with native myocardium, ACS biomaterials science & engineering 6 (5) (2020) 2757–2769, https://doi.org/10.1021/acsbiomaterials.9b01860.
[64] X. Li, X. He, Y. Yin, R. Wu, B. Tian, F. Chen, Administration of signalling molecules dictates stem cell homing for *in situ* regeneration, J. Cell Mol. Med. 21 (2017) 3162–3177, https://doi.org/10.1111/jcmm.13286.
[65] S. Perveen, R. Vanni, M. Lo Iacono, R. Rastaldo, C. Giachino, Direct reprogramming of resident non-myocyte cells and its potential for in vivo cardiac regeneration, Cells 12 (2023) 1166, https://doi.org/10.3390/cells12081166.
[66] H. Yamakawa, Heart regeneration for clinical application update 2016: from induced pluripotent stem cells to direct cardiac reprogramming, Inflamm. Regen. 36 (2016) 23, https://doi.org/10.1186/s41232-016-0028-z.
[67] P. Zhou, W.T. Pu, Recounting cardiac cellular composition, Circ. Res. 118 (2016) 368–370, https://doi.org/10.1161/CIRCRESAHA.116.308139.
[68] S.B. Karch, V. Fineschi, P. Francia, M. Scopetti, M. Padovano, F. Manetti, A. Santurro, P. Frati, M. Volpe, Role of induced pluripotent stem cells in diagnostic cardiology, World J Stem Cells 13 (2021) 331–341, https://doi.org/10.4252/wjsc.v13.i5.331.
[69] M. Abulaiti, Y. Yalikun, K. Murata, A. Sato, M.M. Sami, Y. Sasaki, Y. Fujiwara, K. Minatoya, Y. Shiba, Y. Tanaka, et al., Establishment of a heart-on-a-chip microdevice based on human IPS cells for the evaluation of human heart tissue function, Sci. Rep. 10 (2020) 19201, https://doi.org/10.1038/s41598-020-76062-w.
[70] G. Gilbert, K. Demydenko, E. Dries, R.D. Puertas, X. Jin, K. Sipido, H.L. Roderick, Calcium signaling in cardiomyocyte function, Cold Spring Harb Perspect Biol 12 (2020) a035428, https://doi.org/10.1101/cshperspect.a035428.
[71] T.P. Martin, E.A. MacDonald, A.A.M. Elbassioni, D. O'Toole, A.A.I. Zaeri, S. A. Nicklin, G.A. Gray, C.M. Loughrey, Preclinical models of myocardial infarction: from mechanism to translation, Br. J. Pharmacol. 179 (2022) 770–791, https://doi.org/10.1111/bph.15595.
[72] T. Jia, C. Wang, Z. Han, X. Wang, M. Ding, Q. Wang, Experimental rodent models of cardiovascular diseases, Front. Cardiovasc. Med. 7 (2020), https://doi.org/10.3389/fcvm.2020.588075.
[73] D.S. Burley, S.A. Hamid, G.F. Baxter, Cardioprotective actions of peptide hormones in myocardial ischemia, Heart Fail. Rev. 12 (2007) 279–291, https://doi.org/10.1007/s10741-007-9029-y.
[74] S. Del Ry, M. Cabiati, A. Clerico, Natriuretic Peptide System and the Heart, 2014, pp. 134–143.
[75] C. Calvieri, S. Rubattu, M. Volpe, Molecular mechanisms underlying cardiac antihypertrophic and antifibrotic effects of natriuretic peptides, J. Mol. Med. (Berl.) 90 (2012) 5–13, https://doi.org/10.1007/s00109-011-0801-z.
[76] M. Mukoyama, K. Nakao, K. Obata, M. Jougasaki, M. Yoshimura, E. Morita, K. Hosoda, S. Suga, Y. Ogawa, H. Yasue, et al., Augmented secretion of brain natriuretic peptide in acute myocardial infarction, Biochem. Biophys. Res. Commun. 180 (1991) 431–436, https://doi.org/10.1016/S0006-291X(05)81311-7.
[77] E. Braunwald, Acute coronary syndromes: BNP measurement predicts AMI risk in the elderly, Nat. Rev. Cardiol. 6 (2009) 503–504, https://doi.org/10.1038/nrcardio.2009.118.
[78] I. George, B. Morrow, K. Xu, G.-H. Yi, J. Holmes, E.X. Wu, Z. Li, A.A. Protter, M. C. Oz, J. Wang, Prolonged effects of B-type natriuretic peptide infusion on cardiac remodeling after sustained myocardial injury, Am. J. Physiol. Heart Circ. Physiol. 297 (2009) H708–H717, https://doi.org/10.1152/ajpheart.00661.2008.
[79] I.A. Sergeeva, V.M. Christoffels, Regulation of expression of atrial and brain natriuretic peptide, biomarkers for heart development and disease, Biochim. Biophys. Acta (BBA) - Mol. Basis Dis. 1832 (2013) 2403–2413, https://doi.org/10.1016/j.bbadis.2013.07.003.
[80] S. Ernest, M. Jankowski, S. Mukaddam-Daher, J. Cusson, J. Gutkowska, Altered regulation of natriuretic peptides in the rat heart by prenatal exposure to morphine, J. Physiol. 506 (Pt 3) (1998) 867–874, https://doi.org/10.1111/j.1469-7793.1998.867bv.x.
[81] E.M. Gravallese, Osteopontin: a bridge between bone and the immune system, J. Clin. Investig. 112 (2003) 147–149, https://doi.org/10.1172/JCI19190.
[82] M.C.L. Keith, R. Bolli, String theory" of c-kit ^{pos} cardiac cells, Circ. Res. 116 (2015) 1216–1230, https://doi.org/10.1161/CIRCRESAHA.116.305557.
[83] K. Dergilev, Z. Tsokolaeva, P. Makarevich, I. Beloglazova, E. Zubkova, M. Boldyreva, E. Ratner, D. Dyikanov, M. Menshikov, A. Ovchinnikov, et al., C-kit cardiac progenitor cell based cell sheet improves vascularization and attenuates cardiac remodeling following myocardial infarction in rats, BioMed Res. Int. 2018 (2018) 1–13, https://doi.org/10.1155/2018/3536854.
[84] N. Witman, C. Zhou, N. Grote Beverborg, M. Sahara, K.R. Chien, Cardiac progenitors and paracrine mediators in cardiogenesis and heart regeneration, Semin. Cell Dev. Biol. 100 (2020) 29–51, https://doi.org/10.1016/j.semcdb.2019.10.011.
[85] S. Barreto, L. Hamel, T. Schiatti, Y. Yang, V. George, Cardiac progenitor cells from stem cells: learning from genetics and biomaterials, Cells 8 (2019) 1536, https://doi.org/10.3390/cells8121536.
[86] H. Chen, L. Wang, W. Wang, C. Cheng, Y. Zhang, Y. Zhou, C. Wang, X. Miao, J. Wang, C. Wang, et al., ELABELA and an ELABELA fragment protect against AKI, J. Am. Soc. Nephrol. 28 (2017) 2694–2707, https://doi.org/10.1681/ASN.2016111210.
[87] S. Xing, J.-Z. Tian, S.-H. Yang, X.-T. Huang, Y.-F. Ding, Q.-Y. Lu, J.-S. Yang, W.-J. Yang, Setd4 controlled quiescent C-Kit+ cells contribute to cardiac neovascularization of capillaries beyond activation, Sci. Rep. 11 (2021) 11603, https://doi.org/10.1038/s41598-021-91105-6.
[88] F. Marino, M. Scalise, E. Cianflone, T. Mancuso, I. Aquila, V. Agosti, M. Torella, D. Paolino, V. Mollace, B. Nadal-Ginard, et al., Role of C-kit in myocardial regeneration and aging, Front. Endocrinol. 10 (2019), https://doi.org/10.3389/fendo.2019.00371.
[89] A.P. Beltrami, L. Barlucchi, D. Torella, M. Baker, F. Limana, S. Chimenti, H. Kasahara, M. Rota, E. Musso, K. Urbanek, et al., Adult cardiac stem cells are multipotent and support myocardial regeneration, Cell 114 (2003) 763–776, https://doi.org/10.1016/S0092-8674(03)00687-1.
[90] A. Aries, P. Paradis, C. Lefebvre, R.J. Schwartz, M. Nemer, Essential role of GATA-4 in cell survival and drug-induced cardiotoxicity, Proc. Natl. Acad. Sci. 101 (2004) 6975–6980, https://doi.org/10.1073/pnas.0401833101.
[91] Q. Liang, L.J. De Windt, S.A. Witt, T.R. Kimball, B.E. Markham, J.D. Molkentin, The transcription factors GATA4 and GATA6 regulate cardiomyocyte hypertrophy in vitro and in vivo, J. Biol. Chem. 276 (2001) 30245–30253, https://doi.org/10.1074/jbc.M102174200.
[92] K. Monzen, I. Shiojima, Y. Hiroi, S. Kudoh, T. Oka, E. Takimoto, D. Hayashi, T. Hosoda, A. Habara-Ohkubo, T. Nakaoka, et al., Bone morphogenetic proteins induce cardiomyocyte differentiation through the mitogen-activated protein kinase kinase kinase TAK1 and cardiac transcription factors Csx/Nkx-2.5 and GATA-4, Mol. Cell Biol. 19 (1999) 7096–7105, https://doi.org/10.1128/MCB.19.10.7096.
[93] L.L. Laemmle, J.B. Cohen, J.C. Glorioso, Constitutive expression of GATA4 dramatically increases the cardiogenic potential of D3 mouse embryonic stem cells, Open Biotechnol. J. 10 (2016) 248–257, https://doi.org/10.2174/1874070701610010248.
[94] M.B. Furtado, M.W. Costa, E.A. Pranoto, E. Salimova, A.R. Pinto, N.T. Lam, A. Park, P. Snider, A. Chandran, R.P. Harvey, et al., Cardiogenic genes expressed

in cardiac fibroblasts contribute to heart development and repair, Circ. Res. 114 (2014) 1422–1434, https://doi.org/10.1161/CIRCRESAHA.114.302530.
[95] N. Kawaguchi, A.J. Smith, C.D. Waring, M.K. Hasan, S. Miyamoto, R. Matsuoka, G.M. Ellison, C-kitpos GATA-4 high rat cardiac stem cells foster adult cardiomyocyte survival through IGF-1 paracrine signalling, PLoS One 5 (2010) e14297, https://doi.org/10.1371/journal.pone.0014297.
[96] M. Malek Mohammadi, B. Kattih, A. Grund, N. Froese, M. Korf-Klingebiel, A. Gigina, U. Schrameck, C. Rudat, Q. Liang, A. Kispert, et al., The transcription factor <scp>GATA</Scp> 4 promotes myocardial regeneration in neonatal mice, EMBO Mol. Med. 9 (2017) 265–279, https://doi.org/10.15252/emmm.201606602.
[97] S.M. Kinnunen, M. Tölli, M.J. Välimäki, E. Gao, Z. Szabo, J. Rysä, M.P.A. Ferreira, P. Ohukainen, R. Serpi, A. Correia, et al., Cardiac actions of a small molecule inhibitor targeting GATA4–NKX2-5 interaction, Sci. Rep. 8 (2018) 4611, https://doi.org/10.1038/s41598-018-22830-8.
[98] M.J. Välimäki, R.S. Leigh, S.M. Kinnunen, A.R. March, A.H. de Sande, M. Kinnunen, M. Varjosalo, M. Heinäniemi, B.L. Kaynak, H. Ruskoaho, GATA-targeted compounds modulate cardiac Subtype cell differentiation in dual reporter stem cell line, Stem Cell Res. Ther. 12 (2021) 190, https://doi.org/10.1186/s13287-021-02259-z.
[99] B.A. Afouda, Towards Understanding the gene-specific roles of GATA factors in heart development: does GATA4 lead the way? Int. J. Mol. Sci. 23 (2022) 5255, https://doi.org/10.3390/ijms23095255.
[100] G.M. Dittrich, N. Froese, X. Wang, H. Kroeger, H. Wang, M. Szaroszyk, M. Malek-Mohammadi, J. Cordero, M. Keles, M. Korf-Klingebiel, et al., Fibroblast GATA-4 and GATA-6 promote myocardial adaptation to pressure overload by enhancing cardiac angiogenesis, Basic Res. Cardiol. 116 (2021) 26, https://doi.org/10.1007/s00395-021-00862-y.
[101] T.T. Yang, S.F. Weng, N. Zheng, Q.H. Pan, H.L. Cao, Liang Liu, H.D. Zhang, D. W. Mu, Histopathology mapping of biochemical changes in myocardial infarction by Fourier Transform infrared spectral imaging, Forensic Sci. Int. 207 (2011) e34–e39, https://doi.org/10.1016/j.forsciint.2010.12.005.
[102] A. Mahler, M. Reches, M. Rechter, S. Cohen, E. Rigid Gazit, Self-assembled hydrogel composed of a modified Aromatic Dipeptide, Adv. Mater. 18 (2006) 1365–1370, https://doi.org/10.1002/adma.200501765.
[103] V. Jayawarna, M. Ali, T.A. Jowitt, A.F. Miller, A. Saiani, J.E. Gough, R.V. Ulijn, Nanostructured hydrogels for three-dimensional cell culture through self-assembly of fluorenylmethoxycarbonyl–Dipeptides, Adv. Mater. 18 (2006) 611–614, https://doi.org/10.1002/adma.200501522.
[104] E.V. Alakpa, V. Jayawarna, A. Lampel, K.V. Burgess, C.C. West, S.C.J. Bakker, S. Roy, N. Javid, S. Fleming, D.A. Lamprou, et al., Tunable supramolecular hydrogels for selection of lineage-Guiding Metabolites in stem cell cultures, Chem 1 (2016) 298–319, https://doi.org/10.1016/j.chempr.2016.07.001.
[105] L.R. Caggiano, J.-J. Lee, J.W. Holmes, Surgical reinforcement alters collagen alignment and turnover in healing myocardial infarcts, Am. J. Physiol. Heart Circ. Physiol. 315 (2018) H1041–H1050, https://doi.org/10.1152/ajpheart.00088.2018.
[106] J.-G. He, H.-R. Li, B.-B. Li, Q.-L. Xie, D. Yan, X.-J. Wang, Bone marrow mesenchymal stem cells overexpressing GATA-4 improve cardiac function following myocardial infarction, Perfusion 34 (2019) 696–704, https://doi.org/10.1177/0267659119847442.
[107] M. Gong, M. Wang, J. Xu, B. Yu, Y.-G. Wang, M. Liu, M. Ashraf, M. Xu, Nano-sized extracellular vesicles secreted from GATA-4 modified mesenchymal stem cells promote angiogenesis by delivering let-7 MiRNAs, Cells 11 (2022) 1573, https://doi.org/10.3390/cells11091573.
[108] H.-B. Kwon, S. Wang, C.S.M. Helker, S.J. Rasouli, H.-M. Maischein, S. Offermanns, W. Herzog, D.Y.R. Stainier, In vivo modulation of endothelial polarization by apelin receptor signalling, Nat. Commun. 7 (2016) 11805, https://doi.org/10.1038/ncomms11805.
[109] N. Sultana, L. Zhang, J. Yan, J. Chen, W. Cai, S. Razzaque, D. Jeong, W. Sheng, L. Bu, M. Xu, et al., Resident C-Kit+ cells in the heart are not cardiac stem cells, Nat. Commun. 6 (2015) 8701, https://doi.org/10.1038/ncomms9701.
[110] J.H. van Berlo, O. Kanisicak, M. Maillet, R.J. Vagnozzi, J. Karch, S.-C.J. Lin, R. C. Middleton, E. Marbán, J.D. Molkentin, C-Kit+ cells minimally contribute cardiomyocytes to the heart, Nature 509 (2014) 337–341, https://doi.org/10.1038/nature13309.
[111] L. Bao, Q. Meng, Y. Li, S. Deng, Z. Yu, Z. Liu, L. Zhang, H. Fan, C-kit positive cardiac stem cells and bone marrow–derived mesenchymal stem cells synergistically enhance angiogenesis and improve cardiac function after myocardial infarction in a paracrine manner, J. Card. Fail. 23 (2017) 403–415, https://doi.org/10.1016/j.cardfail.2017.03.002.
[112] N.S. Mabotuwana, L. Rech, J. Lim, S.A. Hardy, L.A. Murtha, P.P. Rainer, A. J. Boyle, Paracrine factors released by stem cells of mesenchymal origin and their effects in cardiovascular disease: a systematic review of pre-clinical studies, Stem Cell Rev Rep 18 (2022) 2606–2628, https://doi.org/10.1007/s12015-022-10429-6.
[113] R. Bolli, S. Ghafghazi, Cell therapy for cardiac repair: what is needed to move forward? Nat. Rev. Cardiol. 14 (2017) 257–258, https://doi.org/10.1038/nrcardio.2017.38.
[114] M. Wysoczynki, A. Khan, R. Bolli, New paradigms in cell therapy, Circ. Res. 123 (2018) 138–158, https://doi.org/10.1161/CIRCRESAHA.118.313251.
[115] T. Eschenhagen, R. Bolli, T. Braun, L.J. Field, B.K. Fleischmann, J. Frisén, M. Giacca, J.M. Hare, S. Houser, R.T. Lee, et al., Cardiomyocyte regeneration, Circulation 136 (2017) 680–686, https://doi.org/10.1161/CIRCULATIONAHA.117.029343.
[116] I. Shiojima, Disruption of coordinated cardiac hypertrophy and angiogenesis contributes to the transition to heart failure, J. Clin. Investig. 115 (2005) 2108–2118, https://doi.org/10.1172/JCI24682.
[117] M. Sano, T. Minamino, H. Toko, H. Miyauchi, M. Orimo, Y. Qin, H. Akazawa, K. Tateno, Y. Kayama, M. Harada, et al., P53-Induced inhibition of hif-1 causes cardiac dysfunction during pressure overload, Nature 446 (2007) 444–448, https://doi.org/10.1038/nature05602.
[118] Y. Izumiya, I. Shiojima, K. Sato, D.B. Sawyer, W.S. Colucci, K. Walsh, Vascular endothelial growth factor blockade promotes the transition from compensatory cardiac hypertrophy to failure in response to pressure overload, Hypertension 47 (2006) 887–893, https://doi.org/10.1161/01.HYP.0000215207.54689.31.
[119] J. Heineke, M. Auger-Messier, J. Xu, T. Oka, M.A. Sargent, A. York, R. Klevitsky, S. Vaikunth, S.A. Duncan, B.J. Aronow, et al., Cardiomyocyte GATA4 functions as a stress-responsive regulator of angiogenesis in the murine heart, J. Clin. Investig. 117 (2007) 3198–3210, https://doi.org/10.1172/JCI32573.